Fluorescence Sensing of Cefixime Antibiotic Using Metal-Organic Framework-Quantum Dots Composite: Synthesis, Characterization and Mechanistic Study

Saba Derakhshan Oskouei

Submitted to the
Institute of Graduate Studies and Research
in partial fulfillment of the requirements for the degree of

Doctor of Philosophy
in
Chemistry

Eastern Mediterranean University
June 2025
Gazimağusa, North Cyprus

Approval of the Institute of Graduate Studies and Research

Prof. Dr. Ali Hakan Ulusoy
Director

I certify that this thesis satisfies all the requirements as a thesis for the degree of Doctor of Philosophy in Chemistry.

Prof. Dr. İzzet Sakallı
Chair, Department of Chemistry

We certify that we have read this thesis and that in our opinion it is fully adequate in scope and quality as a thesis for the degree of Doctor of Philosophy in Chemistry.

Assoc. Prof. Dr. Akeem Adeyemi Oladipo
Co-Supervisor

Prof. Dr. Mustafa Gazi
Supervisor

Examining Committee

1. Prof. Dr. Terin Adalı
2. Prof. Dr. Mustafa Gazi
3. Prof. Dr. İbrahim Volkan Kumbaracı
4. Prof. Dr. Bahire Filiz Şenkal
5. Prof. Dr. Elvan Yılmaz

ABSTRACT

This study successfully designed and fabricated a novel fluorescence-based sensing platform by integrating boron and nitrogen co-doped carbon dots (B,N-CDs) with the UiO-66 metal-organic framework. Comprehensive characterization techniques confirmed the successful synthesis and structural integrity of the hybrid material and verifying the retention of the UiO-66 crystalline framework and the successful doping of B and N elements within the carbon dots.

The resulting B,N-CD@UiO-66 nanocomposite exhibited excellent fluorescence sensing capabilities for cefixime (CFX), demonstrating a low detection limit of 4.21 nM, a broad linear response range of 0–100 nM, and a fast detection time of 4.4 seconds. Fluorescence quenching was primarily governed by static quenching, with a minor contribution from inner filter effects. The sensor showed high selectivity towards CFX and also exhibited remarkable stability, maintaining over 97% of its fluorescence intensity after 60 days, and demonstrated good reusability over multiple sensing cycles. Furthermore, the sensor was successfully applied to detect CFX in complex real samples such as honey, tap water, and seawater, yielding satisfactory recovery rates (96.9% to 101.63%) and low relative standard deviations (1.54% to 5.34%). These results affirm the potential of the B,N-CD@UiO-66 nanocomposite as a versatile and highly sensitive sensing system for practical applications in environmental surveillance, food quality monitoring, and clinical diagnostics.

Keywords: Cefixime Detection; Fluorescence Sensor; Carbon Dots; Metal-organic Framework; B,N Co-doping; Antibiotic Quenching.

ÖZ

Bu çalışma, bor ve azot ile eş katkılanmış karbon noktacıklarının (B,N-CD'ler) UiO-66 metal-organik iskelet (MOF) ile birleştirilmesiyle yenilikçi bir floresans tabanlı algılama platformu tasarlayıp başarıyla üretmiştir. Kapsamlı karakterizasyon teknikleri, hibrit malzemenin başarılı sentezini ve yapısal bütünlüğünü doğrulamış, ayrıca UiO-66'nın kristal yapısının korunduğunu ve karbon noktacıkları içinde B ve N elementlerinin başarıyla katkılandığını teyit etmiştir. Elde edilen B,N-CD@UiO-66 nanokompoziti, sefiksim (CFX) için mükemmel floresans algılama yetenekleri sergilemiştir; 4.21 nM gibi düşük bir tespit limiti, 0–100 nM arasında geniş bir lineer yanıt aralığı ve 4.4 saniye gibi hızlı bir algılama süresi göstermiştir. Floresans söndürme mekanizması esas olarak statik söndürme ile gerçekleşmiş, iç filtre etkilerinin katkısı ise küçük olmuştur. Sensör, CFX'e karşı yüksek seçicilik göstermiştir ve %97'den fazla floresans yoğunluğunu 60 gün sonra bile koruyarak olağanüstü bir stabilite ortaya koymuştur. Ayrıca, çoklu algılama döngülerinde iyi yeniden kullanılabilirlik sergilemiştir. Sensör ayrıca bal, musluk suyu ve deniz suyu gibi karmaşık gerçek örneklerde CFX tespiti için başarıyla uygulanmış; %96.9 ila %101.63 arasında tatmin edici geri kazanım oranları ve %1.54 ila %5.34 arasında düşük bağıl standart sapmalar elde edilmiştir. Bu sonuçlar, B,N-CD@UiO-66 nanokompozitinin çevresel izleme, gıda kalitesi kontrolü ve klinik tanı gibi pratik uygulamalarda kullanılabilecek çok yönlü ve son derece hassas bir algılama sistemi olma potansiyelini doğrulamaktadır.

Anahtar Kelimeler: Sefiksim Tespiti; Floresans Sensör; Karbon Noktacıklar; Metal-organik Iskelet; B,N Eş-doplama; Antibiyotik Söndürme.

DEDICATION

To my beloved and incredible parents, your endless support and unwavering belief were always a source of strength and guiding light throughout this journey. Thank you for always being my rock. And to my precious one and cheerleader Salih Diran, your constant companion, steady hand, and encouraging words empowered me to overcome despair and frustration. This success would not have been possible without your presence on my side.

ACKNOWLEDGMENT

I would like to express my gratitude to my advisor, Prof. Dr. Mustafa Gazi, for their invaluable guidance which has been instrumental in shaping this revised thesis.

I would like to extend my special and heartfelt thanks to my co-supervisor Prof. Dr. Akeem Oladipo for his influential support, wealth of knowledge, and extensive experience which have enriched my academic endeavors. His mentorship has been invaluable in completing this research.

I am also grateful to my fellow lab mates, for their collaborative efforts, and unwavering friendship. Their camaraderie and support have made the challenging times more bearable and the rewarding moments more enjoyable.

I owe my deepest gratitude to the person who stood by me every step of the way, my dearest companion, Salih Diran. His unwavering support, understanding, and presence have made this experience not only bearable but truly meaningful. Without his steadfast support, I could not have overcome the many challenges of these years.

Finally, I am deeply indebted to my beloved parents, Yousef and Farideh. Their sacrifices, love, and guidance have shaped me into the person I am today. Their unwavering support and encouragement have been invaluable throughout my academic journey. I am forever grateful for their love and sacrifices.

TABLE OF CONTENTS

LIST OF TABLES

LIST OF FIGURES

LIST OF ILLUSTRATIONS

Chapter 1

INTRODUCTION

1.1 Background and Significance

Antibiotics are chemical compounds used widely to prevent and treat infectious diseases in humans and livestock. Since Alexander Fleming discovered the first isolated antibiotic, penicillin, in 1928 [1], hundreds of isolated or synthesized antibiotics have been available for human and animal treatments [2]. The global consumption of antibiotics has increased dramatically, with industrialization and the increasing human population. Between 2010 and 2019, the total antibiotic consumption for developed and undeveloped countries was estimated to be around 100,000-200,000 tons [3]. The COVID-19 pandemic that developed in 2019 led to a global surge in antimicrobial consumption. Antibiotic use ranges from 33% in the Western Pacific Region to 83% in the Eastern Mediterranean and African Regions, as the World Health Organization (WHO) reported. Prescriptions dipped in Europe and the Americas from 2020 to 2022 but increased in Africa [4,5].

Since approximately 30% of the ingested antibiotics can be metabolized by humans and animals, the majority is excreted via urine and other excretion pathways unchanged or degraded [6]. Aquatic antibiotic contamination occurs due to incorporating antibiotic residues, effluents from wastewater treatment plants, pharmaceutical industries, hospitals, and run-off from agricultural land.

Cephalosporins belong to the β-lactam antibiotics which represent the most commonly used and prescribed antibiotics worldwide. Frequent detection of these compounds was reported with high concentrations in wastewater, surface water, and seawater [7]. The β-lactam ring structure of Cefixime, a third–generation cephalosporin, makes it resistant to degradation and bioaccumulation. This antibiotic by entering aquatic ecosystems directly and indirectly can alter water quality and affect bacterial colonization in ecosystems [8]. In addition, the accumulation of antibiotics can promote the rapid emergence of antibiotic-resistant bacteria, which prevents the therapeutic efficacy of antibiotics in treating bacterial diseases [9].

Humans can absorb residual antibiotics through the food chain or drinking water, which has the potential to contribute to health problems including cancer, bacterial resistance, liver damage, and allergic reactions. Antimicrobial-resistant bacteria have been detected all over the world and these are currently one of the major threats to public health according to the World Health Organization (WHO) [10]. To address these issues and reduce environmental pollution and ecological risks rapid and straightforward antibiotic monitoring is needed.

1.1.1 Cefixime: Structure, Existence, and Importance of Its Detection

Cefixime, (6R, 7R)-7- [[(Z)-2-(2-Aminothiazol-4-yl)-2-[(carboxymethoxy)imino] acetyl] amino]-3-ethenyl-8-oxo-5-thia-1-azabicyclo [4.2.0] oct- 2-ene-2-carboxylic acid trihydrate, a third generation cephalosporin with oral bioavailability, is widely used in the treatment of urinary tract and respiratory infections, middle ear infections, pharyngitis and tonsillitis. In addition, cefixime possesses activity against pathogenic bacteria such as *Staphylococcus aureus, Anaerobes, Haemophilus influenzae, E. coli, and Meningococcus* [11]. This compound ($C_{16}H_{15}N_5O_7S_2 \cdot 3H_2O$; M.W: 453.45 g/mol) (Figure 1) was obtained semi-synthetically from the marine fungus *Cephalosporium*

acremonium and was approved by the FDA for the first time in 1989. The central structure consists of the 7-Aminocephalosporanic acid with a fused beta-lactam ring to a dihydrothiazine ring [11–13].

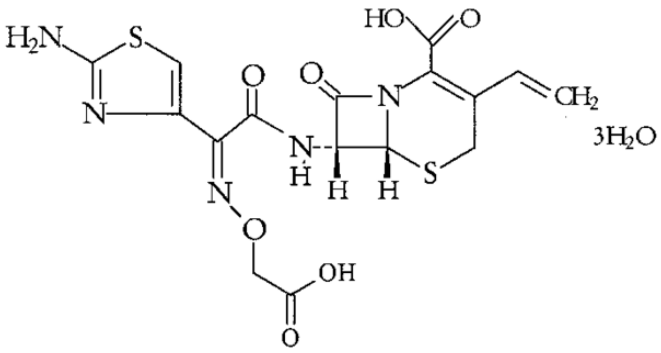

Figure 1: Structural representation of Cefixime

Among the β-lactam class, cefixime has the highest average concentration of 0-1800 ng/L in the effluent of wastewater treatment plants in China [14], and significant concentration between 278.65 and 422.1 ng/l in wastewater in Iran-Tehran [15]. Such increased concentrations of cefixime contribute to antimicrobial resistance development within the respective bacterial population and may also have potential toxic effects on living organisms, ecosystems, and human health. Therefore, it is essential to establish rapid and sensitive methods to detect these pharmaceuticals in the environmental media.

1.1.2 Limitations of Traditional Methods of Antibiotics Quantification

Many advanced analytical methods have been developed for detecting antibiotics in wastewater. Among these, chromatography, mass spectrometry, and capillary electrophoresis stand out as leading instrumental techniques, offering high sensitivity and accuracy.

- Chromatography:

  Liquid chromatography (LC) is currently the most prevalent method for detecting macrolide antibiotics due to its simple operation and rapid analysis. Combined liquid chromatography techniques, such as Liquid Chromatography-Ultraviolet (LC-UV), Liquid Chromatography-Fluorescence (LC-FL), and Liquid Chromatography-Mass Spectrometry (LC-MS), have been successfully developed to analyze a wide range of antibiotics with exceptional selectivity, sensitivity, and accuracy. However, the conventional use of LC for routine residue analysis can sometimes be limited, particularly when dealing with complex matrices, trace-level concentrations, or the need for very high throughput screening. This is often due to extensive sample preparation requirements, potential matrix effects, or the need for highly specialized and costly mass spectrometry detectors for definitive identification and quantification of very low levels [16].

- High-performance liquid chromatography (HPLC)

  HPLC is among the most utilized analytical techniques for nonvolatile pharmaceutical analysis. This technique separates individual components of a mixture depending on how they interact with both the stationery and mobile phases [17,18]. Despite the versatility of chromatography-based analytical techniques for antibiotic detection, the associated instrumentation can be prohibitively costly and sample pretreatment processes are often time-consuming and labor-intensive.

- Mass spectrometry (MS):

  Mass spectrometry (MS), though powerful, is not ideal as a standalone tool for detecting antibiotics in complex matrices like wastewater due to significant matrix interferences. Its true strength lies in coupling with separation techniques such as LC-MS or GC-MS, which isolate target antibiotics from other compounds,

improving selectivity, sensitivity, and accuracy. However, traditional MS-based approaches (e.g., LC-MS/MS, LC-HRMS) have notable limitations for routine environmental monitoring such as high cost, low throughput, matrix effects, and laborious sample prep. These factors limit MS's practicality for large-scale, routine environmental surveillance of antibiotics [19,20].

- Capillary electrophoresis (CE):

  CE is an attractive alternative to chromatographic techniques particularly when the sample quantities are low. The main benefits of CE are its high separation efficiency, lower sample volumes required, lower cost due to minimal organic solvent usage, and cheaper capillary expenses. In addition, CE is analysis able to automation, high-sample-throughput analysis, and multiplexing of detection modes. A major disadvantage of CE is the lack of sensitivity of the method for low concentrations and trace residues due to the small sample injection volumes and the short optical path lengths of the on-capillary detection [21].

Given the inherent limitations of traditional instrumental techniques, there's a pressing need to develop innovative strategies for detecting pollutants across diverse environmental media with improved sensitivity and selectivity. Among various emerging approaches, optical methods, particularly fluorescence-based assays, are highly promising alternatives. They offer fast response times, high accuracy, superior sensitivity, and excellent selectivity, making them a compelling choice for future antibiotic monitoring.

1.1.3 Optical Method: The Promise of Fluorescence-based Sensing

Among various emerging approaches, optical methods, particularly fluorescence-based assays, offer a highly promising alternative. Fluorescence sensing operates by

capturing signals generated from the interaction between a recognition element (like a biomolecule) and a target analyte. This interaction is then transformed into a measurable fluorescence signal, allowing for qualitative and quantitative analysis based on changes in fluorescence intensity, emission wavelength, or lifetime [22]. Historically, fluorescence sensing relied on traditional organic dyes as fluorophores. However, the rapid advancements in nanotechnology have led to the development of novel fluorescent nanomaterials, such as quantum dots (QDs), carbon dots (CDs), upconversion nanoparticles (UCNPs), and metal-organic frameworks (MOFs). These new materials have largely supplanted conventional dyes due to their superior properties, including high fluorescence quantum yield and excellent photostability. This innovation has significantly expanded the prospects for highly sensitive detection of various biochemical molecules [23–25]. Fluorescence-based sensors are recognized as exceptionally promising probes for detecting a wide array of analytes, ranging from ions and small molecules to complex biomolecules. This is largely attributed to their numerous advantages over traditional techniques: low cost, portability, straightforward visualization, ease of preparation, and highly selective and sensitive responses. Given these many advantages of fluorescence sensing over conventional detection methods, this PhD study specifically focuses on developing and applying fluorescence-based methodologies for the sensitive and selective detection of antibiotics in diverse environmental media.

1.2 Overview of Metal-Organic Frameworks (MOFs)

Over the past three decades, porous materials have emerged as a central focus across chemistry, physics, and materials science. Their remarkable diversity in pore orientations, dimensions, shapes, and sizes has made them a subject of intensive and widespread research. The International Union of Pure and Applied Chemistry (IUPAC)

classifies porous materials into three distinct categories based on characteristic pore size: microporous (less than 2 nm), mesoporous (2-50 nm), and macroporous (greater than 50 nm) [26,27].

In 1995, Yaghi's groundbreaking work introduced a novel class of crystalline porous materials known as metal-organic frameworks (MOFs) [28,29]. MOFs are exceptional crystalline hybrid materials, typically micro/mesoporous, constructed through the self-assembly of metal-containing secondary building units (SBUs) and organic linkers. This precise arrangement forms highly ordered one-, two-, and three-dimensional networks characterized by outstanding pore volumes and surface areas. The vast array of available building units and versatile connection modes allows for the synthesis of thousands of different MOFs. Indeed, as of January 2020, the Cambridge Structural Database (CSD), MOF subset alone had cataloged 99,075 unique MOFs, a number that continues to grow steadily [30].

1.2.1 Structure and Properties of MOFs

Metal-organic frameworks (MOFs) are crystalline structures composed of metal ions or clusters, acting as secondary building units (SBUs), linked by organic ligands through coordination bonds and electrostatic interactions. This precise arrangement forms extended networks characterized by well-defined pores and channels. For MOF synthesis, common organic linkers are typically di-, tri- or tetra-dentate ligands, such as carboxylates, phosphonates, sulfonates, and various heterocyclic compounds (Figure 2). The inorganic component, comprising isolated polyhedral or small clusters of metal ions, can exhibit diverse structural geometries. These include linear, T-shaped, Y-shaped, tetrahedral, square planar, square pyramidal, trigonal bipyramidal, octahedral, trigonal prismatic, … arrangements (Figure 3) [26,31–33].

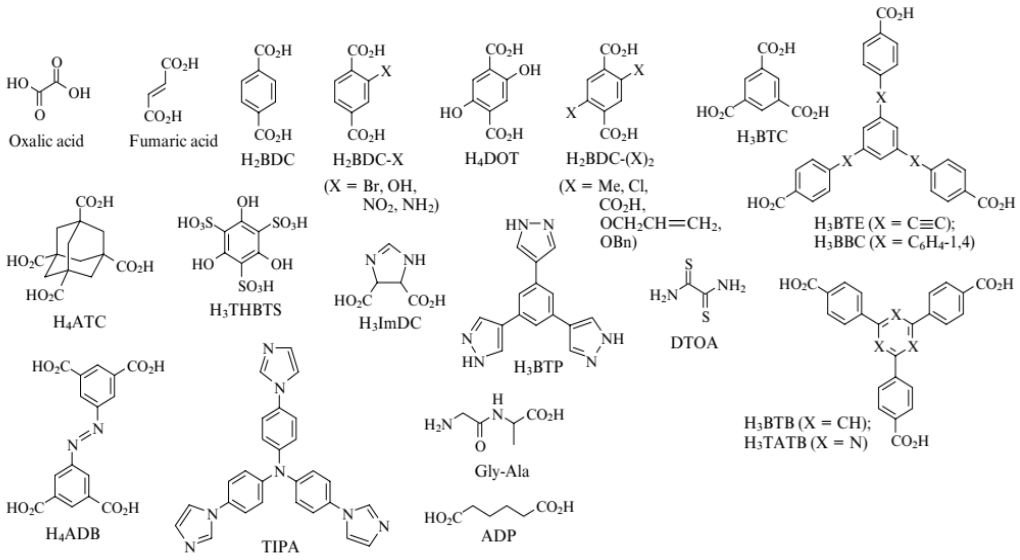

Figure 2: Some examples of organic molecules used as linkers [26]

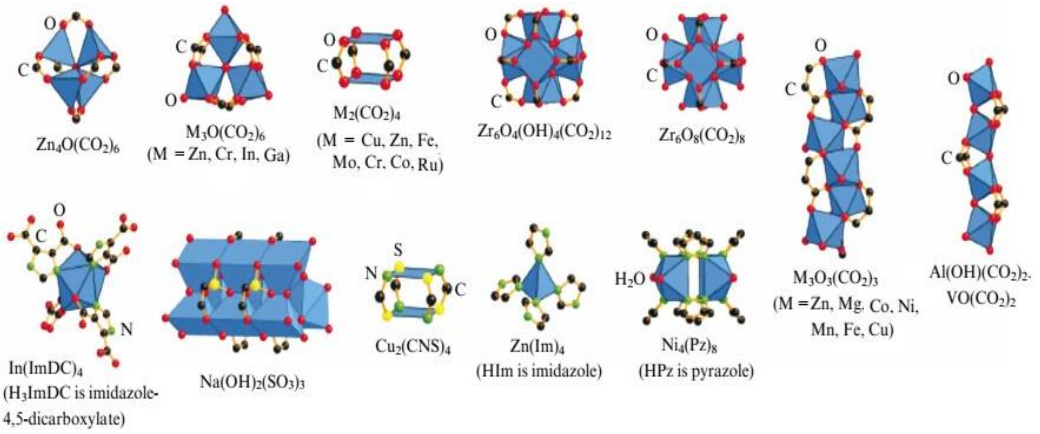

Figure 3: Metal clusters (the polyhedral demonstrate the metal coordination) [26]

MOFs are well known to present remarkable properties including:

- High porosity: The diameters of the pores may even exceed 98 Å [34].
- High surface areas: up to 10,000 m^2/g [35].
- Low framework densities: as low as 0.126 g/cm^{-3} [36].

The remarkable characteristics of MOFs position them as highly promising candidates for a wide array of applications, encompassing adsorption, biomedicine, drug delivery, magnetism, chemical separation, luminescence catalysis, and the removal of toxic

chemicals from water and air [37]. The ability to precisely select different metal clusters and organic linkers allows for deliberate alterations in framework topology, pore volume, pore size, and overall functionality. This enables researchers to design tailored MOFs with specific properties and functions. Furthermore, MOFs can be further functionalized through post-synthetic modification (PSM) methods. This approach involves the chemical modification of organic linkers or SBUs after the initial MOF synthesis, facilitating the incorporation of new types of functional groups into the network. This strategic tuning allows for the optimization of MOF's physical and chemical properties, leading to materials with highly desirable functions [38,39]. Given the vast number of MOFs that can be synthesized and their diverse applications, this study focuses on a specific and highly relevant example: **UiO-66**. UiO-66 stands out due to its exceptional attributes, particularly its high porosity and robust structural stability. This MOF demonstrates remarkable resilience under extreme conditions, including high temperatures and significant chemical pressures, making it an exceptionally favorable material for a wide range of applications [39].

1.2.2 UiO-66: A Promising MOF for Sensing Applications

A notable milestone in materials science occurred in 2008 when researchers at the University of Oslo (UiO) developed a pioneering zirconium-based MOF, designated UiO-66. This robust MOF is constructed from $[Zr_6O_4(OH)_4]$ octahedral clusters connected by twelve 1,4-benzene dicarboxylic acid (H_2BDC) ligands [40,41]. The high coordination number inherent in this structure endows UiO-66 with exceptional thermal and mechanical stability. It remarkably retains its three-dimensional framework even at temperatures up to 500°C and under pressures as high as 1.0 MPa. Furthermore, UiO-66 has been confirmed to maintain its morphology across various solvents, including water, ethanol, dimethylformamide (DMF), benzene, and acetone.

Its strong resistance to both strong acids and partial alkaline conditions further underscores its excellent chemical stability [42]. The intricate cubic crystal structure of UiO-66, characterized by interconnected octahedral and tetrahedral cages, is detailed in Figure 4 [43,44]. With a high Brunauer-Emmett-Teller (BET) surface area range (1100−1200 m^2/g), UiO-66 is highly applicable for numerous advanced applications [45].

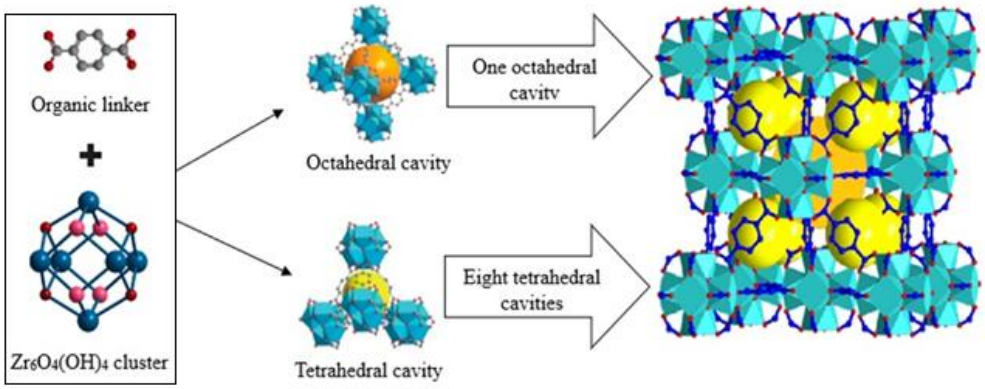

Figure 4: the crystal structure of UiO-66. The yellow spheres display the cavities in the tetrahedral and octahedral cages [43].

While UiO-66 possesses a highly tunable framework structure and exceptional stability, pristine MOFs, when employed in fluorescence sensing, often face inherent limitations such as potential structural collapse under certain conditions and, critically, weakened intrinsic fluorescence intensity. This reduced emission can hinder their direct application for highly sensitive analytical tasks.

To overcome these limitations and enhance their optical performance, post-synthetic modification (PSM) offers a versatile approach. PSM enables the creation of highly functionalized MOF-based composites by encapsulating or integrating various optical guest species within the MOF cavities. These guests include fluorescent dyes, lanthanide metal ions, and notably, carbon-based quantum dots (QDs) [46].

Among these approaches, modification with quantum dots (QDs) has emerged as a particularly advantageous strategy. QDs, due to their unique quantum size effects, offer several benefits: they possess high fluorescence quantum yields, excellent photostability, broad absorption spectra, and narrow, tunable emission spectra. Consequently, quantum dot modification represents a powerful approach to overcoming the fluorescence limitations of pristine MOFs, offering enhanced sensitivity, selectivity, and overall analytical performance for diverse applications.

1.3 Quantum Dots (QDs) and Their Properties

Quantum dots are semiconductor nanocrystals, typically ranging in size from 1 to 10 nm. They bridge the gap between bulk materials and individual atoms, exhibiting unique and tunable optical and electronic properties primarily due to quantum confinement effects [47]. QDs are broadly classified based on their composition. The most common types include: These are often composed of II-VI (e.g., cadmium selenide (CdSe), cadmium sulfide (CdS), III-V (e.g., indium phosphide (InP), gallium arsenide (GaAs), or IV-VI (e.g., lead sulfide (PbS) semiconductor materials, and those based on group IV elements, such as carbon quantum dots, silicon quantum dots, graphene quantum dots, and germanium quantum dots [47,48].

Regardless of their specific composition, QDs are characterized by exceptional optical properties, including strong fluorescence, high photostability (resistance to photobleaching), high brightness, and size-tunable emission spectra. These attributes make them highly suitable for diverse advanced applications such as photodetectors, bioimaging, catalysis, photovoltaics, light-emitting diodes (LEDs), and photoconductors [49].

1.3.1 Structural and Optical Properties of QDs

The remarkable advantages of quantum dots (QDs) in sensing applications stem directly from their unique structural and optical properties, which are governed by the principles of quantum confinement. At the nanoscale, specifically when the particle's radius becomes less than the exciton Bohr radius (the average separation between an excited electron and the resulting hole), the energy levels within these semiconductor nanocrystals become quantized. This quantum confinement fundamentally alters their electronic band structure. When an external energy source, such as ultraviolet (UV) light, excites an electron from valence band to conduction band, fluorescence occurs upon the electron's relaxation back to its ground state and recombination with the hole. This process releases energy in the form of light. Crucially, the energy released during this relaxation process is directly dependent on the bandgap of the quantum dot material. As the particle's size decreases, the energy gap between the valence and conduction bands expands, as illustrated in Figure 5. Consequently, more energy is required to excite electrons, and subsequently, more energy is released during their relaxation, leading to a blue shift (emission of shorter wavelength light) in the emitted fluorescence [50,51]. This size-tunable emission, coupled with strong fluorescence, high photostability, makes QDs exceptionally versatile and powerful fluorophores for diverse sensing applications.

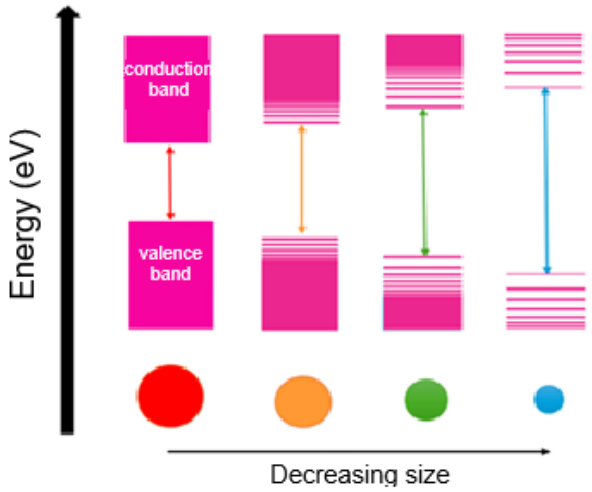

Figure 5: Energy level diagram of QDs

Smaller QDs, typically with radii less than 2-3 nm, emit shorter wavelength light, resulting in fluorescent colors ranging from violet to blue or green. Conversely, larger QDs, with radii approaching 5-6 nm, emit longer wavelength light, corresponding to colors in the yellow, orange, or red regions of the spectrum (Figure 6). This remarkable size-tunable emission characteristic enables QDs to span a wide spectrum of colors, simply by precise control of their dimensions during synthesis [52–54].

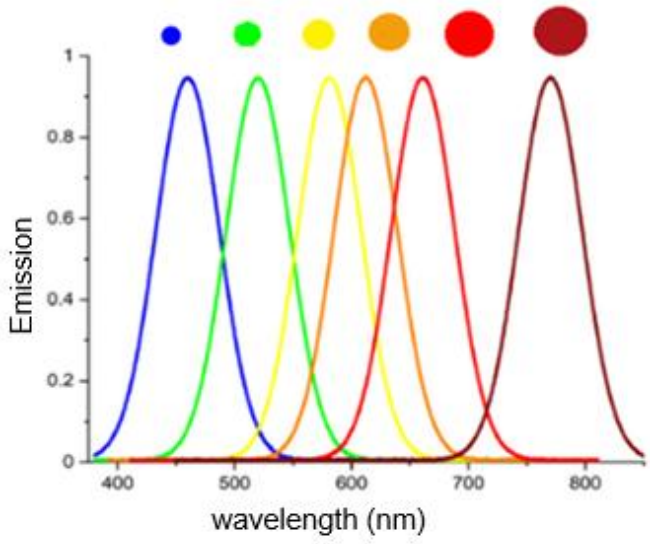

Figure 6: fluorescence spectra of QDs and their sizes

Beyond their tunable emission, QDs also exhibit exceptional photostability and resistance to photobleaching. This high photochemical stability, particularly when compared to conventional organic fluorophores, offers a significant advantage, enabling more accurate and sensitive detection in various applications, including demanding scenarios like clinical diagnostics [55,56].

1.3.2 Application of Quantum Dots in Fluorescence Sensing

Quantum dots (QDs), as highly luminescent nanomaterials, are exceptionally well-suited for diverse fluorescence sensing applications. Their superior optical properties, including high photostability, broad absorption spectra, narrow and symmetric emission bands, and large Stokes shifts, enable highly effective detection of various analytes [57,58]. The sensing efficiency of QD-based sensors can be substantially enhanced through precise structural modifications. These include tailoring the nanocrystal's size, morphology, and composition, introducing dopants, and performing surface functionalization [59,60]. The successful development of high-performance QD-based sensors, however, fundamentally relies on a thorough understanding of the underlying detection mechanisms. Fluorescence sensing with QDs typically operates via interactions between the QD and the target analyte leading to changes in the QD's fluorescence intensity. These changes are often mediated by various quenching mechanisms, which include:

- Static quenching: Formation of a non-fluorescent complex between the QDs and the analyte.
- Dynamic quenching: Collisional deactivation of excited QD by the analyte.
- Photoinduced electron transfer (PET): Electron transfer between the excited QD and the analyte.

- Inner Filter Effect (IFE): Absorption of excitation or emission light by the analyte or other components in the sample, reducing the fluorescence intensity.
- Aggregation-caused signal changes: Analyte-induced aggregation or dispersion of QDs leading to fluorescence modulation.
- Energy transfer: Non-radiative energy transfer from the QD (donor) to the analyte (acceptor), such as Förster Resonance Energy Transfer (FRET), Surface Energy Transfer (SET), or Dexter Energy Transfer [61–63].

Among the various strategies for developing QD-based fluorescence sensors, the modification of MOFs with quantum dots stands out as a particularly compelling approach. The synergistic combination of MOFs with QDs leads to enhanced analytical performance, making QD-modified MOFs promising platforms for the selective and sensitive detection of antibiotics in complex environmental matrices.

1.4 Objectives of the Study

This PhD study aims to address the limitations of traditional antibiotic detection methods and conventional fluorescence sensors by developing a novel, highly sensitive, and selective hybrid fluorescence sensing platform. The objectives are:

- To design and synthesize a novel class of co-doped carbon-based quantum dots (CQDs) featuring heteroatoms, specifically Boron (B) and Nitrogen (N).

The inclusion of B and N as co-dopants is hypothesized to strategically alter the electronic structure of the CQDs, enhancing their intrinsic fluorescence quantum yield, photostability, and providing additional active sites for selective interaction with target analytes, thereby overcoming the limitations of traditional carbon-based quantum dots.

- To develop a novel hybrid fluorescence sensor by incorporating the synthesized B,N-co-doped CQDs within the framework of UiO-66 MOF that leverage the superior

optical properties of the co-doped CQDs while exploiting the high surface area, tunable pore structure, and robust chemical stability of UiO-66. This approach eliminates the inherent limitations of both pristine UiO-66 (e.g., weak intrinsic fluorescence) and standalone carbon-based quantum dots (e.g., agglomeration, reduced stability in complex matrices), yielding a synergistic sensing platform.

- To evaluate the performance of the developed B,N-co-doped@UiO-66 hybrid fluorescence sensor for the sensitive and selective detection of Cefixime by determining critical analytical parameters such as linearity, limit of detection (LOD), and selectivity in artificially contaminated water samples (laboratory setting) and extending to real environmental and biological media (e.g., wastewater effluents, urine, serum).
- To investigate and elucidate the underlying fluorescence quenching mechanism(s) involved in the interaction between the hybrid sensor and Cefixime.
- To assess the reusability and regeneration capabilities of the developed B,N-co-doped@UiO-66 MOF hybrid sensor to ascertain its long-term applicability and practical utility for sustainable environmental and biological monitoring.

1.5 Thesis Outline

This thesis is structured into five chapters.

- Chapter 1 details the critical issue of antibiotic pollution in environmental media and outlines the inherent limitations of conventional analytical methods for their detection. It then introduces fluorescence-based sensing materials, particularly metal-organic frameworks (MOFs) and quantum dots (QDs), as highly promising alternatives for sensitive and selective antibiotic quantification.
- Chapter 2 provides a comprehensive overview of the fundamental properties and applications of fluorescence-based sensors utilizing MOFs and carbon-based quantum

dots (CQDs). This chapter specifically highlights the significant advantages offered by hybrid composites, focusing on the potential of B,N-co-doped CQDs@UiO-66 for enhanced sensing performance.

- Chapter 3 meticulously describes the synthetic procedures employed for novel B,N-co-doped CQDs and their integration into the UiO-66 framework. It also details the analytical techniques used for material characterization and the methodologies for conducting fluorescence quenching studies.
- In Chapter 4, the discussion centers on the structural, morphological, and optical characterization results of the synthesized composites. This chapter thoroughly elucidates the fluorescence sensing mechanisms involved in the detection of antibiotics.
- Finally, Chapter 5 summarizes the main research findings of this study and outlines potential future research directions within this evolving field.

Chapter 2

LITERATURE REVIEW

2.1 Fluorescence-based Sensing of Antibiotic

Fluorescence analysis stands as a powerful analytical tool, widely recognized for its rapid response, high sensitivity, and cost-effectiveness [64,65]. Significant advancements in tailoring appropriate fluorescence probes have propelled the development of rapid, in-situ, and ultrasensitive methods for determining target analytes. This progress greatly expands the potential of fluorescence-based techniques for diverse practical applications. At its core, fluorescence detection transduces analyte information, such as concentration, into quantifiable fluorescence signals. This is achieved by utilizing specific recognition components that interact with the analyte, leading to a measurable modulation of fluorescence intensity, lifetime, or emission wavelength, thereby enabling both qualitative and quantitative detection [66,67].

Fluorescence sensing modes are generally categorized into three principal types based on their signal response: fluorescence quenching (turn-off sensing), where the signal decreases upon analyte interaction; fluorescence enhancement (turn-on sensing), where the signal increases; and ratiometric fluorescence, which involves monitoring the ratio of two fluorescence signals for improved accuracy and robustness [68] .

2.1.1 Nanomaterials in Fluorescence-based Antibiotic Sensing

The development of fluorescence-based antibiotic sensors has seen a surge in the utilization of various nanomaterials, leveraging their unique properties to significantly enhance sensor performance. These materials include quantum dots (QDs), metal-

organic frameworks (MOFs), metal nanoclusters (NCs), and other nanostructures such as silica nanoparticles, silver nanoparticles, gold nanoparticles, nanotubes, and upconversion nanoparticles [69]. Among these materials, QDs and MOFs stand out:

Quantum Dots (QDs):

Quantum dots, as highly luminescent semiconductor nanocrystals, have garnered immense interest as emitters in direct-binding sensors due to their superior optical properties. A diverse range of QDs, including carbon dots [70,71], silicon quantum dots [72,73], various doped QDs [74,75], and chalcogenide QDs [76,77], exhibit size-tunable emission spectra and robust photophysical characteristics, making them highly promising candidates for both sensing and imaging applications. For instance, sulfur quantum dots have proven effective for detecting antibiotics in food samples. Lu et al. (2021) reported the use of SQDs for determining trace amounts of tetracycline in milk, achieving a Limit of Detection (LOD) of 28 nM within a dynamic concentration range of 0.1–50 μM [78]. Similarly, chalcogenide quantum dots (e.g., CdS, CdSe, CdTe, and ZnS) are extensively employed in fluorescence-based sensing owing to their excellent optical properties. An example includes the CdSe/CdS quantum dot-based sensor developed by Hou et al. for detecting sparfloxacin in milk, which achieved an LOD of 0.1391 ppm over a concentration range of 0.5–30 ppm [79].

Metal-Organic Frameworks (MOFs) Nanomaterials:

Metal-organic frameworks have been widely explored as advanced sensing platforms for antibiotics due to their high tunability, porous structures, and chemical versatility. MOFs based on various metal centers, including Zn-based [80,81], Zr-based [82], Al-based [83], and Cd-based MOFs [84,85], have demonstrated excellent performance in terms of sensitivity, specificity, and stability for antibiotic detection. For example, Li et al. developed an NH_2-MIL-53(Al) MOF-based nanosensor for the ultrasensitive

determination of tetracycline in milk samples [83]. The high efficiency of this sensor was primarily attributed to the dense distribution of $-NH_2$ and −COOH functional groups on the MOF's surface, which facilitated hydrogen bonding with the −CO− and −OH groups of tetracycline molecules. This interaction led to the formation of an NH_2 -MIL-53(Al)-TC complex, causing fluorescence quenching of the MOF predominantly through the inner filter effect (IFE) and photoinduced electron transfer (PET) mechanisms.

2.1.2 Challenges and Limitations of Existing Fluorescent Sensors

Despite the significant progress in fluorescence-based antibiotic sensing, several challenges persist, hindering their widespread application. While QDs are promising candidates for luminescence-based antibiotic sensing due to high sensitivity, fast response time, and relatively facile synthesis, their practical application is often limited by their instability under various environmental conditions, which can compromise sensor performance and reliability. Moreover, the inherent toxicities associated with heavy metal-based QDs, such as CdTe, CdSe, CdS, and $CsPbBr_3$, raise serious concerns, particularly for applications involving food safety and biological samples [69]. Addressing these issues necessitates further research into developing more stable, biocompatible, and eco-friendly QDs, improving their specificity and affordability.

MOF-based sensors offer a compelling platform for sensitive, rapid, and easily implementable real-time monitoring of antibiotics. However, to fully realize their potential in practical applications, future investigations are crucial to improve their performance in diverse and complex sample matrices, enhance their stability in aqueous environments (especially under acidic conditions), and address challenges regarding their specificity and cost-efficiency. Overcoming these hurdles is critical for

the development of robust and effective MOF-based nanosensors capable of sensitive antibiotic detection in real-world samples [86].

2.2 Metal-Organic Framework (MOFs) in Sensing Applications

MOF-based fluorescent sensors represent a cost-effective, simple, and highly sensitive approach for detecting various analytes, making them suitable for rapid analysis and trace detection. Among these, Luminescent Metal-Organic Frameworks (LMOFs), a specialized class of MOFs, have garnered considerable attention for their substantial potential in fluorescence sensing [87]. Their luminescence properties originate from several distinct mechanisms:

- **Organic Ligand Luminescence:** This is the most prevalent emission origin, typically observed in LMOF systems incorporating extended π-conjugated organic ligands. The luminescence arises from the excited states of the organic linkers themselves.
- **Metal-Center Luminescence (Antenna Effect):** This mechanism is commonly observed in LMOFs composed of specific metal ions, where the organic ligands act as "antennas" to absorb excitation energy and transfer it to the luminescent metal center. This phenomenon is prominent in MOFs containing:
    - Rare earth ions (Lanthanides) such as Eu, Pr, Tb, Tm, Sm, and Nd [88].
    - Transition metals: Fe, Cu, Ag, Zn, Cd, Co, Mn [89].
    - Heterometal-organic frameworks: Systems combining d-block and f-block metals within a single MOF, exemplified by Ce-Ag and Eu-Cd ions integrated with polydentate ligands containing nitrogen and oxygen donor atoms [90,91].
    - Main group MOFs: MOFs incorporating main group metals like bismuth, lead, indium, and magnesium [92,93].

- **Charge Transfer Luminescence:** This mechanism involves the transfer of electrons between the ligand and the metal center, encompassing both ligand-to-metal charge transfer (LMCT) and metal-to-ligand charge transfer (MLCT) processes [94].
- **Guest-Induced Luminescence:** In this scenario, luminescent guest species are strategically encapsulated within the MOF structure to impart or enhance their luminescence performance. Common guest species include carbon quantum dots [95,96] and various fluorescent dyes [97–99].

MOF-based fluorescent sensors have attracted considerable interest specifically for the detection of antibiotics. Such sensors typically operate via fluorescence quenching (turn-off sensing), fluorescence enhancement (turn-on sensing), or a ratiometric method (involving both increase and decrease) in response to varying concentrations of the analyte [100]. While developing highly sensitive and selective turn-on sensors remains a more challenging task [101], fluorescence quenching is an extensively utilized and effective strategy. For example, fluorescence quenching can occur through mechanisms such as the inner filter effect (IFE), photoinduced electron transfer (PET), or fluorescence resonance energy transfer (FRET) [102]. By thoroughly understanding these fluorescence principles and exploring different design routes, it is possible to engineer highly selective, specific, and practical MOF-based sensors for numerous antibiotic detection applications.

2.2.1 MOFs as Platforms for Analyte Capture and Detection of Antibiotics

Metal-organic frameworks (MOFs) offer significant advantages over traditional adsorbents like zeolites and activated carbon due to their exceptionally high surface area, intrinsic porosity, and remarkable structural tunability. These characteristics

make MOFs particularly well-suited for enhancing the efficiency of wastewater treatment processes [103]. Adsorption, a widely employed and cost-effective technology for pollutant removal from water, is favored for its simplicity, low operational cost, and minimal generation of secondary pollution. The adsorption process typically involves three key steps: (1) diffusion of the contaminant to the surface of the adsorbent, (2) subsequent diffusion of the contaminant into the internal pores of the adsorbent, and (3) eventual binding of the contaminant onto active sites through various host-guest interactions [104]. More specifically, the adsorption of antibiotics by MOFs is a complex process driven by a combination of both physical and chemical interactions. Physical adsorption mechanisms include electrostatic forces (especially relevant for charged species) and dispersion forces (van der Waals interactions). Conversely, chemical adsorption results from the formation of stronger chemical bonds between the MOF and the antibiotic molecule. MOF-based materials generally leverage a multitude of synergistic mechanisms for antibiotic capture, encompassing hydrophobic interactions, electrostatic attractions, acid-base interactions, hydrogen bonding, and π-π stacking interactions (Figure 7) [105,106].

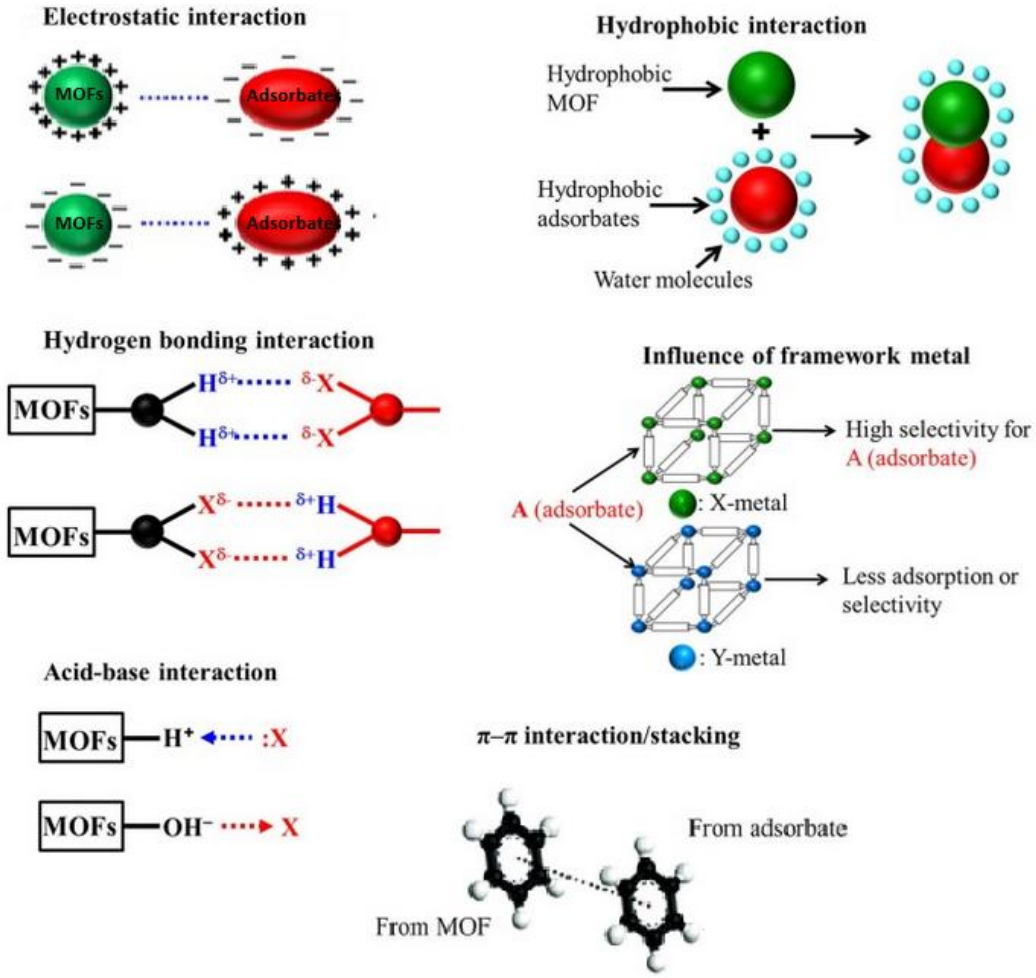

Figure 7: Possible mechanisms of adsorbates on MOFs [106]

The host–guest interactions and adsorption performance of metal-organic frameworks (MOFs) can be effectively tailored through rational material design. Strategies such as pore size enlargement, incorporation of functional groups, metal doping, and formation of composite structures have been widely employed to enhance the adsorption capacity and selectivity of MOFs for targeted applications [104,107].

An increasing number of research studies have shown that UiO-66 MOF is highly effective in fluorescent sensing as potent material for the adsorption and detection of antibiotics in aqueous media, even at trace levels.

2.2.2 UiO-66-based sensors

Owing to its tunable porosity, UiO-66 serves as an excellent adsorbent in sensing applications. Additionally, functionalized UiO-66 MOF has demonstrated great potential in fluorescence-based detection systems [108–110].

Adsorption application: With its high chemical and water stability, remarkable compatibility, and certain physicochemical properties including high porosity, great surface area, as well as adjustable pore size, UiO-66 has become a potential adsorbent, and by modeling the structure and constructing defects in the MOF structure, the number of adsorption sites can be increased. Since the pristine UiO-66 framework possesses many open metal sites and π-π interactions, contaminants with charge or benzene ring structures can be efficiently adsorbed [111,112]. In addition, the excellent compatibility of UiO-66 also makes it a suitable platform for modification with functional materials or modifiers. When functional groups, such as $-NH_2$, -OH, or $-SO_3H$ are introduced into the UiO-66 frame, the number of active sites increases, improving their adsorption capacity. These functional groups can facilitate contaminant interactions via several mechanisms such as electrostatic attraction, chelation, and hydrogen bonding [113,114]. Li et al. investigated the absorption of metronidazole from water onto UiO-66 and UiO-66-NH_2 in 2019 [115]. To enhance the adsorption capacity of metronidazole by UiO-66, the researchers added amine functional groups to the framework. Hydrogen bonding and electrostatic interactions were found to play significant roles in the increased amount of adsorbed metronidazole. Experimental maximum adsorption capacities of 200.2 mg g^{-1} for unmodified UiO-66 and 265.5 mg g^{-1} for amine functionalized UiO-66-NH_2 were obtained.

Several methods have been developed to introduce structural defects in the UiO-66 framework to improve the pore diameter and adsorption capacity. One effective approach is doping UiO-66 with metal ions, such as Co, Eu, Hf, Ce, Ti, and La. The formation of unsaturated coordination sites via this doping process could significantly enhance adsorption performance [116–118]. A series of Hf-UiO-66 and Ti-UiO-66 were synthesized in 2022 via a post-synthetic approach to increase cephalosporin uptake [119]. Introducing Hf/Ti as dopants in UiO-66 generated defects and modified surface charges, offering enlarged pores and greatly enhanced adsorption capacities.

The construction of composites is a promising approach to integrating the benefits of multiple components and overcoming their drawbacks[120,121]. In 2020, Tao et al. reported an efficient tetracycline adsorption using a UiO-66-$(COOH)_2$/GO composite [122]. The composite showed a maximum adsorption capacity of 164.91 mg/g, much higher than that for pristine UiO-66 (27.53 mg/g). The improved performance is due to the synergistic effect of GO and carboxyl groups, which supply more active sites for tetracycline binding. The adsorption mechanism involves a combination of π-π stacking between tetracycline aromatic rings with GO, chemical coordination with the exposed metal centers of UiO-66, and weak electrostatic interactions.

Fluorescence sensing application: The fluorescence sensing ability of Zirconium-based MOFs is an efficient and rapid approach to identifying contaminants in water. Pristine UiO-66 has weak fluorescence properties due to LMCT, however, it is structurally stable and tunable allowing modification of the metal center and the organic ligand, accordingly, leading to increased specific fluorescence responses [43]. UiO-66-NH_2 synthesized by Wang et al. with rich -NH_2 groups on its surface, which could have further improved its water stability and offered binding sites for target tetracycline [123]. This sensor exhibits good fluorescence properties quenched by

tetracycline via PET and IFE. The strong hydrogen bonding of amino groups on UiO-66-NH_2 and the hydroxyl groups of tetracycline allows for selective determination of analyte from other interferences with the LOD of 0.449 μM.

Although UiO-66-based MOFs have broad applications such as antibiotic detection and removal, there may be some disadvantages related to their practical applications. Such drawbacks can be mitigated by using functionalization with amines, carboxylic acids, or phosphoric acids and hybridization with carbon nanotubes, nanoparticles, or graphene so that their properties for specific applications can be tailored. In this way, by improving stability, selectivity, and adsorption capacity, these engineered MOFs can provide advanced solutions for environmental remediation and other applications.

2.3 Carbon Dots (CDs) in Fluorescence Sensing

Carbon dots emerging as a new class of biosensors, have unique properties such as inherent fluorescence, high surface-to-volume ratio, resistance to photobleaching, surface tunability, and various precursor options. Due to these qualities, CDs excel in different fields such as clinical diagnostics, forensics, medicine, food, drug analysis, and other biosensing applications [124,125]. Several factors, such as surface functionalization, CD size, and excitation wavelength may modulate the fluorescence behaviors of CDs. Understanding such complex interactions is crucial for optimizing applications based on CDs, especially in sensing, bioimaging, and optoelectronics.

2.3.1 CDs Properties and Advantages

Carbon dots (CDs) are zero-dimensional photoluminescence nanomaterials with intrinsic fluorescence properties and typically have less than 10 nm diameters. Based on the elemental composition and optical properties, such predominant types of carbon dots can be divided into three widespread species as presented in Figure 8: (1)

graphene quantum dots (GQDs), (2) carbon quantum dots (CQDs), nanodots (CNDs) and (3) polymer dots (PDs) [126]. CNDs are amorphous and do not possess a well-defined crystal lattice, thereby, do not show quantum-confinement effects. On the other hand, GQDs, in which multiple layers of graphene are stacked and functionalized with surface groups, show quantum confinement effects [126,127]. The CQDs have a hybrid structure of crystalline and amorphous domains. The builders of the CQDs are a graphitic core (composed of pervasive sp^2-hybridized carbon atoms) that underlines the optical and electronic properties.

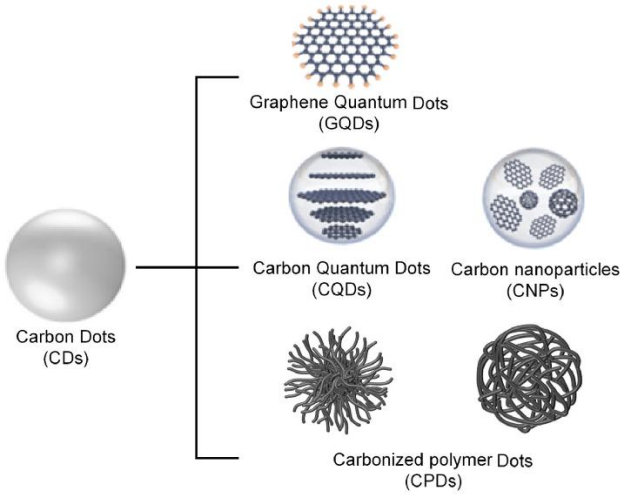

Figure 8: Classification of carbon dots and their structures [51]

CDs have low molecular weight and quasi-spherical shape and display quantum confinement effects [128]. The fluorescence properties of CDs originate from:

- **The carbon-core states** are obtained from the separation of valence and conduction bands of the graphene-like core; thus, it is important for the fluorescence behavior of CDs, especially for larger-sized CDs [129,130].
- **Surface defect states**: these defects are induced by different surface functional groups, such as hydroxyl, carboxyl, and amine groups (Figure 9) [131]. Such defects serve as emission centers and lead to various fluorescence manifests,

such as multicolor emission and excitation-dependent fluorescence. These functional groups are also responsible for their great solubility and biocompatibility in water, enabling the graft of biomolecules, polymers, or other moieties, and offer expanded functionalities [132,133]. On the other hand, doping with heteroatoms (i.e., N, S, and B) can enhance the radiative recombination and improve these surface defect states' fluorescence intensity and quantum yield [134,135].

- **Molecular states** originate from fluorophores or chromophores located on the surface of the CD. These states act like organic dyes, allowing sharp and intense fluorescence with high quantum yield, although they possess relatively low photostability [134].

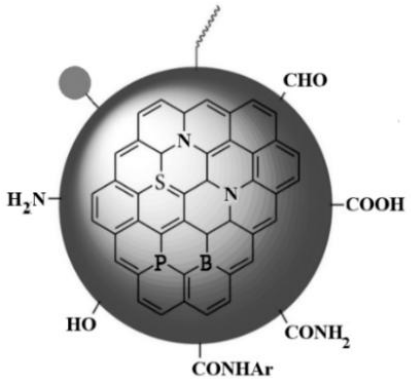

Figure 9: General structure of carbon quantum dots [136]

The precursors for synthesizing CDs can be of both chemical and biological origin. Some popular chemical precursors are glucose, sucrose, citric acid, lactic acid, ascorbic acid, glycerol, and ethylene glycol [137–142]. Natural sources, including Artocarpus lakoocha seeds, rice husks, Azadirachta indica leaves, pomelo peel, Ficus benghalensis latex, and aloe vera have all been used [143–147]. They focus on friendly techniques that reduce the reliance on harmful and toxic substances. Different

synthesis methods of CDs greatly affect their final properties, resulting in different chemical characteristics. Due to their intrinsic bandgap structure, carbon dots possess specific properties, including low toxicity, low cost, excellent biocompatibility, and unique optical and electronic properties, making them promising candidates for bioimaging and other biomedical applications [148,149].

2.3.2 Application of CDs in Antibiotic Detection

Due to their unique optical properties and versatility, CDs have great potential for diverse sensing applications, including detecting molecular targets such as DNA, proteins, antibiotics, and metal ions. Fluorescence quenching, one of the most widespread mechanisms used in CD sensors, is based on the quenching of CD fluorescence upon interaction with analytes [124,150–152]. The quenching can be contact-based mechanisms such as static quenching [153], dynamic quenching [154], photoinduced electron transfer (PET) [155], or noncontact-based mechanisms such as the inner filter effect (IFE), fluorescence resonance energy transfer (FRET), and chemiluminescence resonance energy transfer (CRET). These mechanisms depend on energy-transfer processes rather than direct electron transfer.

By selecting proper adsorbent-analyte pairs, researchers can develop sensors for sensing various analytes. By understanding these mechanisms and designing the experimental conditions appropriately, CQDs can be explored as versatile and sensitive probes for various analytical applications.

2.4 MOF@CD Composites for Sensing

Metal-organic frameworks (MOFs) have large specific surface areas, tunable pore sizes, and diverse functional groups, rendering them selective adsorbents for different pollutants, such as antibiotics. However, conventional synthesis methods generally

lead to powdered MOF crystals, making these materials non-processable, and limiting their practical use as adsorbents [156,157]. On the other hand, as luminescence sensors, they also have a low quantum yield [158]. Thus, host-guest assembly strategies have been proposed as a useful strategy to solve this problem. Fluorescent guest species can be encapsulated in the voids of these MOFs to provide composite materials with superior fluorescence performance [159,160]. MOF-based composites can be prepared using different materials, including metal nanoparticles, organic polymers, silica, and quantum dots. Carbon dots, especially, as a novel class of carbon nanomaterials, have attracted wide attention due to their excellent biocompatibility and thermal stability, low toxicity, unique optical properties, and high photostability [161,162]. Nevertheless, macromolecular impurities, excitation intensity, and probe concentration interferences often limit the detection accuracy of CDs as fluorescent probes. Moreover, large amounts of CDs cause aggregation and collision between particles in the solid state, resulting in high aggregation-induced quenching and low photoluminescent quantum yield [158]. Thus, the encapsulation of CDs in porous materials such as metal-organic frameworks and the preparation of MOF@CDs composite materials should be a valid solution to accomplish the combination of positive traits of single components and the minimization of their deficiencies.

2.4.1 Synergistic Effects of MOFs and CDs

Sensors based on MOF@CDs composites utilize the combined CDs optical characteristics and MOF adsorptive features, resulting in advantageous sensing performance [163,164]. That renders versatile applications possible for MOF@CDs. MOFs play an important role in the sensing process by:

Enhanced adsorption: With their variety of pore structures and large surface area, MOFs can efficiently capture target analytes, resulting in improved sensitivity.

Selective binding: MOF has open metal sites and functional groups in their framework, including Lewis acidic or basic sites, that can selectively bind analytes, enhancing selective detection.

Size-selective diffusion: MOFs' hierarchical porosity allows only the molecules with the proper sizes to access the active sites, enhancing the selectivity.

On the other hand, incorporating CDs enables fine-tuning of MOF@CDs composites in terms of optical properties. The functional groups on the surface of CDs can act as target analyte binding sites, which also play an important role in enhancing sensing performance [165]. Thus, the synergistic effects between MOFs and CDs have raised sensitivity and selectivity, which render MOF@CDs composites perfect candidates for sensing. The interaction between CDs and MOFs adjusts the fluorescence intensity and the excitation wavelength of MOF@CDs composites. This phenomenon is related to the altered electronic transition between surface groups of CD and MOF components, leading to a red or blue shift in the emission spectrum. The tunable fluorescence characteristics render the MOF@CDs composites versatile materials in fluorescence sensing [166].

2.4.2 Recent Advances in MOF@CDs-based Sensors

Due to their sensitive, fast response and specific sensing ability, MOF@CDs sensors are potential antibiotics detection platforms in medicine and pharmacy. For example, Fu et al. reported CDs@Eu-MOF sensors synthesized by doping blue emissive CDs as target receptors in the cavity of red-light Eu-MOFs that can detect doxycycline [167] through FRET mechanism, which means energy transferred from the excited CDs to the target molecule. Simultaneously, it was reported that the cooperation between doxycycline and Eu^{3+} ions promoted the fluorescence intensity of Eu^{3+} at 616 nm.

Overall, this dual effect of the target on the sensor resulted in a visible color change from blue to red.

Wu et al. synthesized the green carbon dot/UiO-66 (g-CD/UiO-66) composite, using solvothermal method. They used this sensor as a ratiometric fluorescent probe for highly sensitive detection of norfloxacin in milk and pork samples. Norfloxacin molecules were absorbed onto the g-CDs@UiO-66 composite surface via hydrogen bonding, which enhances the electrostatic repulsion between the composite particles increasing the fluorescence intensity even in the presence of other interfering substances. The fluorescence probe exhibited high selectivity and sensitivity, with a limit of detection (LOD) of 0.082 μM in a wide linear range of 1-8 μM.

It was believed that understanding the MOF@CDs composites topic requires elaborating on more advanced methods for their synthesis and the scope of their application. Future studies will undoubtedly offer guidelines for the rational design and scaled-up application of these materials.

Chapter 3

MATERIALS AND METHODS

3.1 Materials

3.1.1 Chemicals and Reagents

Chemicals from Sigma Aldrich (Darmstadt, Germany) are zirconium tetrachloride ($ZrCl_4$, > 99.5%), terephthalic acid (C_6H_4-1,4-$(CO_2H)_2$, 98%), sodium hydroxide (NaOH, ACS reagent, ≥97%, pellets) and N, N-dimethylformamide anhydrous (DMF, 99.8%). Citric acid monohydrate ($CH_2COOH.H_2O$,99.5%) and boric acid (H_3BO_3, 61.84%) were purchased from British Drug Houses (England). The Cefixime antibiotic used in this study was obtained from a pharmacy in Iran. Urea ($CO(NH_2)_2$, ACS reagent, 99.0-100.5%) and hydrochloric acid (HCl, 37% solution in water) were acquired from Merck KGaA (Germany). All the reagents used in the present study were analytical pure grade and were used without further purification.

3.1.2 Equipment

Characterizations were performed at Ataturk University (Turkey) as follows:

The materials were characterized by powder X-ray diffraction using PANalytical Empyrean XRD. Brunauer-Emmett-Teller (BET) surface area characterization obtained using Micromeritics 3 flex BET apparatus. The scanning electron microscopy (SEM) analysis utilized Zeiss Sigma 300 coupled with energy-dispersive X-ray spectroscopy. The operation of TEM images of synthesized materials was performed by Hitachi High-tech HT7700 (Japan). X-ray photoelectron spectroscopy (XPS) data was obtained with a Specs-flex XPS microprobe. Other characterization techniques

were performed at Eastern Mediterranean University: FTIR spectroscopy (PerkinElmer, UK), Ultraviolet-visible spectroscopy (T90+, PG Instruments LTD, UK), and Fluorescence Spectroscopy (Hitachi FL-4600).

3.2 Synthesis of UiO-66

UiO-66 crystals were synthesized using the solvothermal method as mentioned in reported literatures, a mixture of zirconium tetrachloride (1.86 g) and 1,4-benzene dicarboxylic acid (BDC) (1.845 g) was first dissolved in 60 ml of N-N′-dimethylformamide (DMF) [168]. After that, 6ml modulator concentrated hydrochloric acid (37%) was added into the mixture solution and stirred vigorously with a magnetic stirrer for 30 min at room temperature. The resulting reaction mixture was then loaded into a Teflon-lined stainless-steel autoclave and kept in a muffle furnace at 120°C for 12 h. The white precipitate was collected after the solution was cooled to room temperature, centrifuged, and washed consecutively three times with DMF, ethanol, and distilled water. The precipitated UiO-66 solid was collected and subsequently left to dry overnight in a vacuum oven at 80°C.

3.3 Synthesis of B,N-codoped Carbon Dots

To prepare the CDs as reported in previous studies [169], a mixture of 0.5 g of citric acid, 0.5 g of boric acid, and 0.25 g of urea was vigorously stirred in 50 ml of ethanol for 30 min in an air atmosphere, then the homogeneous solution was transferred into 100 ml of Teflon lined stainless steel autoclave and so treated in a muffle furnace at 180°C for 12 h. After the reaction was completed, the reaction mixture was directly cooled down to room temperature. Then, the solution was purified by the filter membrane (0.22 μm) to remove unreacted reagents. The filtered CDs were dialyzed by 75Da, MWCO membrane against ethanol for 12 h and the obtained solution was stored and kept in a refrigerator.

3.4 Synthesis of UiO-66@B,N-CD Composite

For preparing UiO-66@B,N-CD composite through in-situ method 50 mL of ethanol was added to 0.5 g of pre-prepared UiO-66 and immersed in 0.5 g of citric acid, 0.5 g of boric acid, and 0.25 g of urea. After stirring for 30 min, the solution was placed in a Teflon-lined stainless-steel autoclave and heated at 180°C for 12 h. After cooling to room temperature naturally, the accumulated solution was washed several times with an ethanol and water mixture and left overnight to dry at 70°C under vacuum.

The in-situ synthesis technique promotes the growth of B,N-doped carbon dots within the pores of pre-formed UiO-66 MOF, which results in intimate contact between the CDs and the MOF framework. This close contact increases the interfacial area and creates strong interactions between them, possibly increasing the stability and sensing ability of the resulting nanocomposite.

To assess the influence of synthesis technique on stability, a control experiment was achieved through mechanical mixing of B,N-CDs with pre-prepared UiO-66 MOF. The composite exhibited a fast decrease in fluorescence response within three days due to aggregation caused by weak interactions and quenching. In contrast, the in-situ synthesized B,N-CD@UiO-66 nanocomposite was very stable, and it maintained its fluorescence for 60 days. This improved stability is due to intense electrostatic, hydrogen bonding, and π-π interactions between the UiO-66 framework and the B,N-CDs that prevent leaching and degradation.

3.5 Characterization Techniques

3.5.1 Powder X-ray Diffraction (PXRD)

The crystalline structure and phase of the prepared materials was characterized by powder X-ray diffraction using a Bruker D8 ADVANCE diffractometer (Germany) equipped with a Cu-Kα radiation (λ = 1.542 nm, 40 kV, 30 mA).

3.5.2 Brunauer-Emmett-Teller (BET)

Micromeritics 3flex BET (USA) apparatus was used to measure the specific surface area, pore volume and pore size of the prepared samples.

3.5.3 Scanning Electron Microscopy (SEM)

The morphology and structure of the prepared samples were studied using a field-emission scanning electron microscopy (Thermo Fisher Scientific, USA) combined with an Energy dispersive X-ray spectroscopy (EDS) device at a potential of 15 kV.

3.5.4 Transmission Electron Microscopy (TEM)

The structure and morphologies of materials were confirmed via a Hitachi High-Tech HT7700 (Japan) transmission electron microscope operated at an accelerating voltage of 40–120 kV.

3.5.5 X-ray Photoelectron Spectra (XPS)

The binding energies of chemical components were determined through the X-ray photoelectron spectra of a Specs-flex XPS Microprobe equipped with a monochromatized Al-Kα X-ray source (1486.71 eV).

3.5.6 Fourier-Transform Infrared Spectroscopy (FTIR)

FTIR spectroscopy was initially employed to obtain the spectra of the samples on the FTIR-8700 spectrophotometer (Perkin-Elmer, UK) between 4000-400 cm^{-1} to identify the functional groups in the samples.

3.5.7 UV-Vis Spectroscopy

UV-vis spectra of samples were monitored on UV–Vis Spectrophotometer (Hitachi U-3010, UK).

3.5.8 Fluorescence Spectroscopy

Fluorescence excitation/emission spectra were recorded on Hitachi Fl4700 spectrophotometer with a 150 W xenon lamp as the light source, using the excitation wavelength at 325 nm.

3.5.9 Nuclear Magnetic Resonance (NMR)

The ^{1}H and ^{13}C NMR spectra of samples were recorded on a Bruker DRX-500 MHz spectrometer (Billerica, MA, USA), using tetramethyl silane as the internal reference and DMSO-d_6 as the solvent.

3.5.10 Photoluminescence (PL) Spectroscopy

photoluminescence spectra measurements were performed with DongWoo SC-100FS fluorescence spectrometer (South Korea), covering temperatures from 77-297 K.

3.6 Fluorescence Sensing Experiments

3.6.1 Fluorescence Sensing of Cefixime

We prepared the B,N-CD@UiO-66 suspension by dispersing 3.0 mg of the nanocomposite in 1 mL of 0.1 M phosphate buffer solution (PBS, pH=7.0). To ensure homogeneity, we subjected this suspension to ultrasonic stirring for 30 min. The fluorescence intensity of this stable suspension served as our control. For cefixime (CFX) detection, we prepared a series of CFX solutions with concentrations ranging from 0.1 nM to 150 μM using deionized water. Next, we added 25 μL of each CFX solution to 175 μL of the stable B,N-CD@UiO-66 suspension, followed by gentle swirling. Then, we recorded fluorescence emission spectra using an excitation wavelength of 330 nm. The fluorescence intensity at 430 nm was recorded once the emission stabilized. We then constructed a standard curve by plotting fluorescence intensity (Y-axis) against the corresponding CFX concentration (X-axis). All

experiments were performed in quadruplicate, and we used the average of these data points for subsequent analysis.

3.6.2 Selectivity, Anti-interference and pH Effect Studies

Initially, the impact of pH on the nanocomposite's fluorescence response was evaluated across a range from 2.9 to 10. All subsequent experiments were performed at the determined optimal pH. To investigate antibiotic interferences, Aqueous solutions of several antibiotics (metronidazole, amoxicillin, tetracycline, ciprofloxacin, and cefuroxime) were prepared at a concentration of 1 mM. For each test, 30 µL of an interfering antibiotic solution was added to 170 µL of a B,N-CD@UiO-66 suspension containing 0.1 mM CFX. After 10 min of ultrasonic stirring, the fluorescence intensity of each resulting mixture was measured.

To assess metal ion interference, aqueous solutions of various metal ions (Cu^{2+}, K^{+}, Mg^{2+}, Ca^{2+}, Mn^{2+}, Ag^{+}, Fe^{3+}, Ni^{2+}, Fe^{2+}) were prepared at a concentration of 1 mM using deionized water. Then, 30 µL of an interfering metal ion solution was added to 170 µL of a B,N-CD@UiO-66 suspension containing 0.1 mM CFX. Following 10 min of ultrasonic stirring, the fluorescence intensity of each mixture was recorded.

Control experiments were conducted to provide baseline data. This involved adding the same volumes of individual antibiotic and metal ion solutions to the B,N-CD@UiO-66 suspension in the absence of CFX. Additionally, the effect of a mixture of interfering species, both with and without CFX, was investigated. All experiments were performed in quadruplicate to ensure accuracy and reproducibility of the results.

3.6.3 Real-Sample Analysis

To assess the practical applicability of the developed B,N-CD@UiO-66 nanocomposite fluorescent probe, we selected various real-world samples, including

seawater, tap water, urine, and honey. Seawater and tap water samples were analyzed directly without any prior treatment. Honey samples underwent a fifty-fold dilution with 0.1 M phosphate buffer solution (pH=7.0). Subsequently, 0.2 μM of CFX was spiked into the diluted honey. The resulting mixtures were then centrifuged at 3000 rpm for 10 min, and the supernatants were used for fluorescence measurements. Fresh urine samples were collected from a healthy individual and centrifuged at 3000 rpm for 10 min to remove impurities. The supernatant was then used. For all sample types, initial fluorescence spectra were recorded without spiked CFX to serve as blank measurements.

Chapter 4

RESULTS AND DISCUSSION

4.1 Probable Synthesis Mechanisms of Materials

The development of the novel B,N-CD@UiO-66 Metal-Organic Framework (MOF) hybrid nanocomposite involves a synergistic combined one-pot approach, leveraging the unique properties of both components. This section details the synthesis mechanism, emphasizing the roles of the dopants and the integration process.

4.1.1 Synthesis of B,N-Codoped Carbon Dots (CDs)

The B,N-codoped CDs were synthesized via a facile hydrothermal carbonization method, utilizing citric acid as the primary carbon source, urea as the nitrogen (N) dopant and surface passivating agent, and boric acid as the boron (B) dopant.

Possible reactions and mechanism:

1. **Carbon core formation:** Under hydrothermal conditions, citric acid undergoes dehydration and carbonization, forming a carbonaceous core. This process involves the breakdown of organic molecules into smaller carbon fragments that then polymerize and condense.

$$C_6H_8O_7 \xrightarrow{\text{Hydrothermal}} \text{carbonaceous precursors} + H_2O + \text{other volatile byproducts}$$

2. **Nitrogen doping and surface passivation:** Urea ($CO(NH_2)_2$) plays a dual role. Upon heating, urea decomposes to release ammonia (NH_3) and isocyanic acid (HNCO). These nitrogen-containing species react with the growing carbon core, leading to the incorporation of nitrogen atoms into the carbon lattice (e.g., pyridinic-

N, pyrrolic-N, graphitic-N) and/or forming nitrogen-containing functional groups on the CD surface (e.g., $-NH_2$, $-CONH_2$).

$$CO(NH_2)_2 \xrightarrow{\Delta} NH_3 + HNCO$$

$$\text{Carbonaceous precursors} + NH_3 / HNCO \xrightarrow{doping/passivation} \text{N-doped CDs}$$

Nitrogen doping is crucial for enhancing the intrinsic fluorescence quantum yield of CDs by creating new energy states within the bandgap and improving surface passivation, which reduces non-radiative recombination pathways.

3. **Boron doping:** Boric acid (H_3BO_3) serves as the boron source. Boron atoms can be incorporated into the carbon framework, typically substituting carbon atoms (e.g., forming B−C bonds) or existing as B−O species on the surface. Boron, being electron-deficient, can significantly influence the electronic structure of the CDs, further tune their optical properties and potentially create Lewis acidic sites that are beneficial for sensing applications. The co-doping of B and N synergistically optimizes the electronic band structure and surface chemistry of the CDs, leading to enhanced fluorescence intensity, improved photostability, and tunable emission wavelengths. These dopants also introduce specific active sites that can interact selectively with target analytes, improving the sensitivity and selectivity of the fluorescence sensor.

$$\text{Carbonaceous precursors} + H_3BO_3 \xrightarrow{Dopping} \text{B-doped CDs}$$

The combined presence of B and N leads to B,N-codoped CDs, exhibiting superior fluorescence properties compared to singly doped or undoped CDs.

4.1.2 Synthesis of UiO-66 MOF

The UiO-66 MOF is synthesized via a standard solvothermal method in a solvent, typically N,N-dimethylformamide (DMF).

Possible reactions and mechanism:

1. **Precursor dissolution:** Zirconium precursor ($ZrCl_4$) and 1,4-benzenedicarboxylic acid (H_2BDC) are dissolved in DMF.

2. **Formation of secondary building units (SBUs):** Under solvothermal conditions (elevated temperature and pressure), the zirconium precursor undergoes hydrolysis and condensation to robust octahedral zirconium clusters, $[Zr_6O_4(OH)_4]^{12+}$ based on HCl modulator. These clusters act as the inorganic secondary building units of the MOF.

$$\text{Zr (IV) precursors} + H_2O \xrightarrow{\text{solvothermal}} [Zr_6O_4(OH)_4]^{12+} \text{ clusters}$$

3. **Coordination and framework assembly:** The H_2BDC ligands (which deprotonate to form BDC^{2-} under reaction conditions) then coordinate with the $[Zr_6O_4(OH)_4]^{12+}$ SBUs. Each SBU connects to twelve BDC^{2-} linkers, forming a highly stable, three-dimensional cubic crystal structure with well-defined octahedral and tetrahedral cages characteristic of UiO-66. The strong Zr-O bonds contribute significantly to the exceptional thermal and chemical stability of UiO-66.

$$[Zr_6O_4(OH)_4]^{12+} + 12\ BDC^{2-} \xrightarrow{\text{coordination}} \text{UiO-66 MOF framework}$$

4.1.3 Synthesis of B,N-Codoped CD@UiO-66 MOF Nanocomposite

The integration of B,N-CDs with the UiO-66 to form the B,N-CD@UiO-66 nanocomposite was achieved through post-synthetic impregnation.

Possible Integration Mechanisms:

The pre-synthesized UiO-66 MOF was introduced into a dispersion of the citric acid, urea and boric acid which led to formed CDs adsorption as guests onto the internal and external surfaces of the porous UiO-66 framework through various non-covalent interactions, possibly based on:

- **Pore confinement:** The porous structure of UiO-66 physically encapsulates and stabilizes the B,N-CDs, preventing their aggregation and enhancing their photostability, which is a common issue for standalone CDs in solution.

- **Hydrogen bonding:** The hydroxyl (-OH) groups on the UiO-66 clusters (from $[Zr_6O_4(OH)_4]$) and the carboxylic acid groups of the BDC^{2-} linkers formed hydrogen bonds with the oxygen- and nitrogen-containing functional groups present on the surface of the B,N-codoped CDs.
- **Electrostatic interactions:** Electrostatic interactions between negatively charged B,N-CD functional groups (-COOH, -OH, $-NH_2$) and Zr^{4+} sites of the UiO-66 framework.
- **π-π Stacking:** The aromatic rings of the H_2BDC linkers in UiO-66 can engage in π-π stacking interactions with the graphitic domains of the B,N-CDs, further enhancing the binding affinity.

Synergistic fluorescence sensing: The integrated hybrid nanocomposite leverages the high fluorescence quantum yield and tunable emission of the B,N-codoped CDs, while the MOF framework provides a robust, porous, and chemically stable platform that can pre-concentrate target antibiotics within its pores. This pre-concentration effect, combined with the specific interactions between the antibiotic and the functionalized CDs (e.g., through electron transfer or energy transfer mechanisms), leads to highly sensitive and selective fluorescence sensing. The MOF acts as a protective and enhancing scaffold for the fluorescent CDs, overcoming the limitations of both individual components and enabling superior performance in complex environmental and biological media.

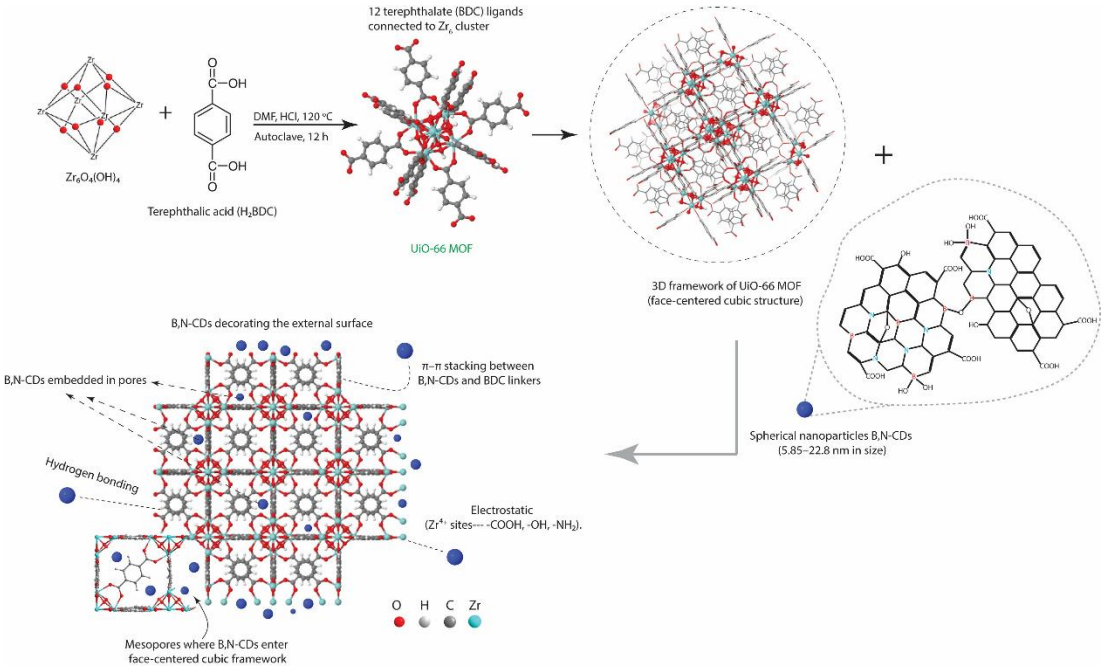

Scheme 1: Probable synthesis mechanism of the B,N-CD@UiO-66 MOF

4.2 Morphological and Surface Characterization

4.2.1 Brunauer-Emmett-Teller (BET)

As shown in Figure 10a, the N_2 adsorption/desorption isotherm of UiO- 66 displays a Type I profile, typical of microporous materials [170,171]. The sharp uptake at low relative pressure (p/p◦) indicates abundant micropores (<2 nm) [172], attributed to the crystalline framework of UiO-66. BET analysis revealed a high surface area of 423.9 m^2/g (Langmuir: 766.5 m^2/g), with a micropore area of 274.1 m^2/g and volume of 0.1345 cm^3/g. The external surface area was 149.8 m^2/g, total pore volume 0.2733 cm^3/g, and average pore size 2.58 nm. The small particle size (14.15 nm) enhances surface accessibility, while a slight curvature at higher pressures suggests minor mesoporosity. The N_2 adsorption/desorption isotherm of B,N-CD shows a Type I profile and microporosity (Figure 10b). The sharp uptake at low relative pressures indicates the presence of micropores formed via small cavities and interconnected channels during synthesis. BET analysis reveals a surface area of 65.46 m^2/g, with a

micropore area of 20.39 m^2/g and external surface area of 45.07 m^2/g. The total pore volume is 0.0286 cm^3/g, and the average pore size of 1.75 nm further confirms the microporous nature.

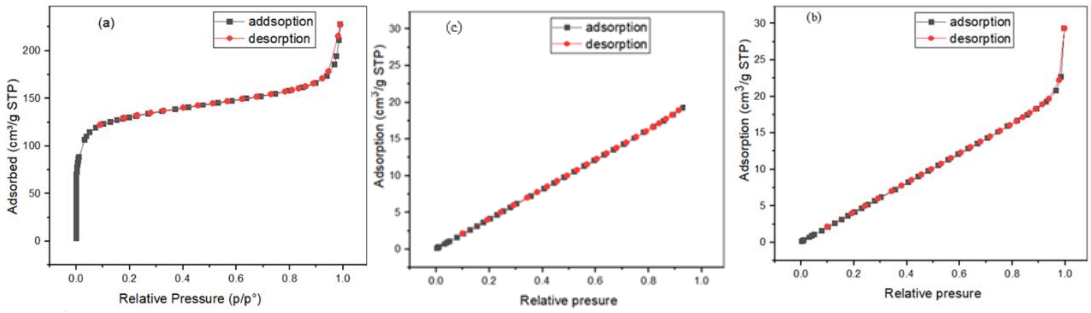

Figure 10: Adsorption-desorption isotherm of (a) UiO-66, (b) B,N-CD and (c) B,N-CD@UiO-66

The N_2 adsorption/desorption isotherm of B,N-CD@UiO-66 shows a Type IV isotherm with a hysteresis loop, indicative of mesoporosity and ink-bottle-type pores (Figure 10c). A sharp uptake at high relative pressure confirms mesopores (2–50 nm) [173,174], likely introduced by B,N-CD integration into the UiO-66 framework. This incorporation may generate voids or interconnect carbon dot networks, enhancing mesoporosity beyond that of pristine UiO-66. The nanocomposite exhibits a BET surface area of 35.63 m^2/g, external surface area of 46.09 m^2/g, pore volume of 0.03105 cm^3/g, and an average pore size of 3.49 nm. The larger average particle size (168.4 nm) suggests some degree of aggregation upon composite formation.

4.2.2 Scanning Electron Microscopy (SEM)

The FE-SEM image (Figure 11a) shows UiO-66 MOF with a dense network of interconnected, polyhedral particles exhibiting characteristic octahedral morphology [172]. The agglomerated structure features rough surfaces and interparticle voids, indicating high porosity and surface area. Particle size analysis via ImageJ revealed sizes ranging from 5.85 to 22.8 nm, with an average of 15.3 nm, aligning with BET

results. These observations confirm the formation of a robust, porous, and crystalline UiO-66 framework.

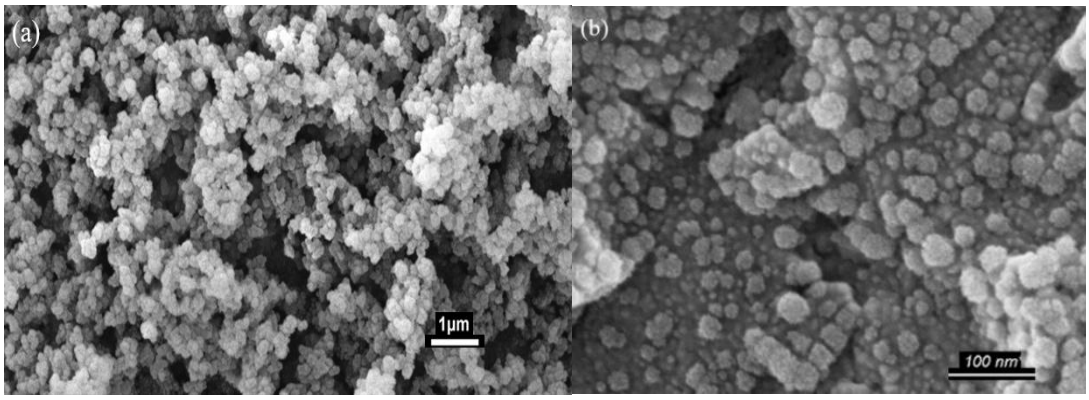

Figure 11: SEM images of (a) UiO-66 and (b) CD@UiO-66

The FE-SEM image (Figure 11b) shows the B,N-CD@UiO-66 nanocomposite with a well-dispersed, heterogeneous morphology. The UiO-66 framework appears as aggregated clusters with a rough, porous surface, while uniformly distributed B,N-CDs impart a granular texture, increasing surface roughness. This integration forms a hierarchical porous structure that may enhance electron transfer, suggesting synergistic interactions between B,N-CDs and UiO-66 potentially improving catalytic, sensing, and adsorption performance over pristine UiO-66.

4.2.3 Transmission Electron Microscopy (TEM)

The TEM image (Figure 12a) shows uniformly dispersed, quasi-spherical B,N-CDs with minimal aggregation. The particles exhibit a narrow size distribution, predominantly below 10 nm, consistent with typical bottom-up synthesis methods. The clear contrast and defined edges confirm the electron-dense nature of the doped carbon cores, while the uniform shape and dispersion suggest good colloidal stability, likely due to surface functionalization from B and N co-doping. The absence of larger clusters indicates effective passivation and stabilization. No distinct lattice fringes are

observed, indicating an amorphous or low-crystalline structure common in heteroatom-doped CDs where B and N introduce defects and functional groups (e.g., B–O, B–N, C–N), disrupting graphitic order. This amorphous nature enhances surface states, which is beneficial for optical applications.

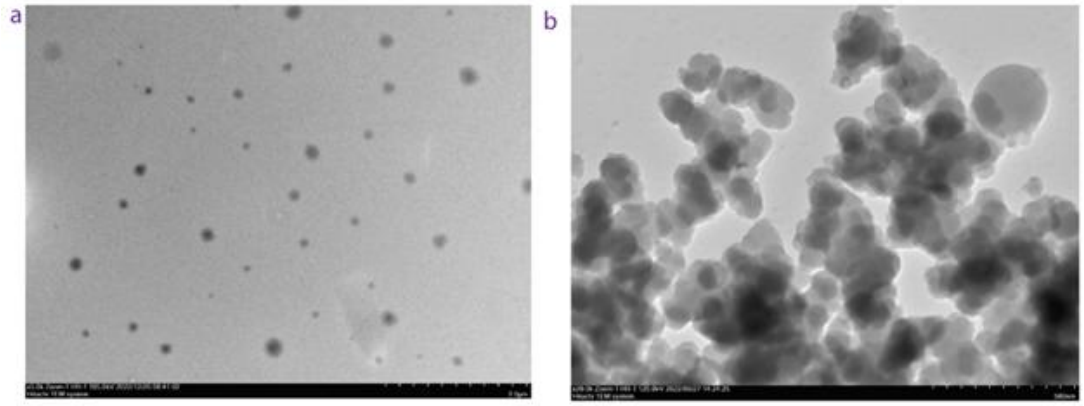

Figure 12: TEM images of (a) B,N-CD and (b) B,N-CD@UiO-66

In contrast, the TEM image of the B,N-CD@UiO-66 nanocomposite (Figure 12b) revealed a more complex and heterogeneous morphology. The UiO-66 MOF framework remained evident, but the incorporation of B,N-CD resulted in a granular appearance due to the presence of finely dispersed B,N-CD particles. Some B,N-CD appeared embedded within the MOF pores, while others were located on the MOF surface. This intimate interaction between B,NCD and the UiO-66 MOF led to the formation of a hierarchical structure with enhanced surface roughness. This morphology suggests a successful integration of B,N-CD within the MOF framework, resulting in a composite material with a complex and heterogeneous structure.

4.2.4 Energy-Dispersive X-ray Spectroscopy (EDS)

Energy-dispersive X-ray spectroscopy (EDS) analysis of the B,NCD@UiO-66 nanocomposite (Figure 13) confirmed the presence of expected elements (C: 19.65 wt. %, O:36.46 wt. %; Zr:31.71 wt. %; B:3.63 % and N: 8.54 wt. %). A weak peak

corresponding to boron (B) and nitrogen (N) in the low-energy region provided evidence for the successful doping of carbon dots. The presence of a strong peak at approximately 2.0 keV confirmed the presence of zirconium (Zr), a key component of the UiO-66 framework. A prominent peak at around 0.28 keV indicated the presence of carbon, originating from both the carbon dots and the terephthalic acid linker of the UiO-66 MOF. The relative intensities of these peaks aligned with the expected elemental composition of the B,N-CD@UiO-66 nanocomposite.

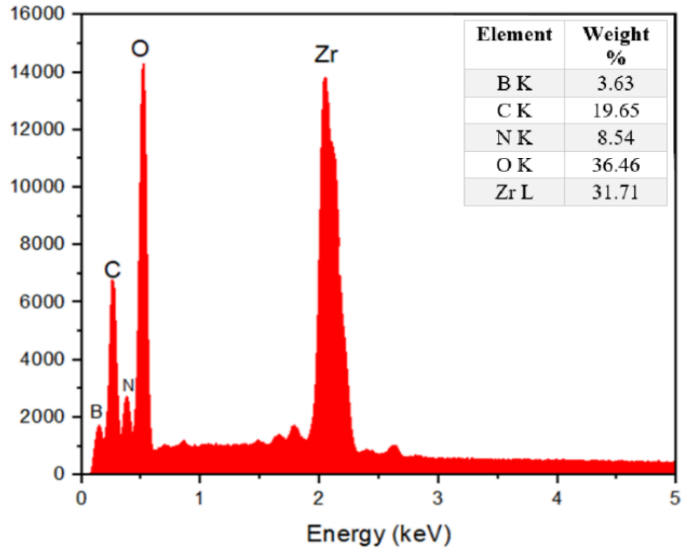

Figure 13: EDX spectra of UiO-66 and CD@UiO-66 composite

4.3 Structural and Compositional Characterization

4.3.1 X-ray Diffraction (XRD)

The XRD pattern of the B,N-CD displayed a broad, diffuse peak spanning 2θ=10˚-25˚, which is characteristic of amorphous carbon materials (Figure 14). This broadness indicates a disordered arrangement of carbon atoms and a lack of long-range structural order. However, the two less prominent peaks were distinguishable. The peak at 2θ=10.44˚ is likely due to the interlayer spacing within turbostratic carbon regions or partially exfoliated graphitic layers [175]. This suggests a larger d-spacing **(**0.75 A˚**)**

than typically found in graphitic materials, possibly resulting from structural distortions caused by the incorporation of boron and nitrogen. The second peak, observed at 2θ=21.53˚ (corresponding to a d-spacing of 3.75 A˚), represents the (002) plane of graphitic carbon. Its shift compared to the typical (002) peak for pure graphite (around 25˚) further indicates the presence of defects or structural distortions within the graphitic framework [175,176]. Collectively, the XRD pattern confirms that the B,N-CD possesses an amorphous nature while also containing graphitic-like domains.

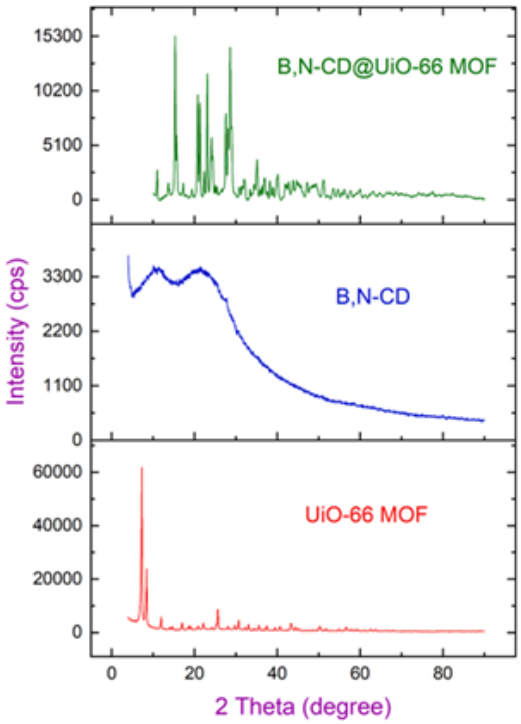

Figure 14: XRD of the synthesized materials

The XRD pattern of the UiO-66 MOF revealed a series of sharp and distinct diffraction peaks, indicative of its highly ordered, crystalline structure. Prominent diffraction peaks at low 2θ angles (approximately 7˚–10˚) signify long-range order within the UiO-66 framework, aligning with reflections from planes such as (111), (200), (220), and (600). This observed pattern closely matched the simulated data (CCDC No. 837,796) [177], confirming the successful formation of the anticipated face-centered

cubic (fcc) structure. Peaks at higher angles (e.g., 15˚–40˚) stemmed from smaller periodicities within the framework, attributed to zirconium (Zr) clusters and their organic linkers. The absence of significant peak broadening or amorphous humps, along with a calculated crystallinity of 89.7%, underscored its high degree of crystallinity and minimal structural imperfections. The crystallite size, calculated using the Scherrer equation based on the most intense (111) peak, was determined to be 89.95 nm. The observed diffraction pattern aligns well with previously reported patterns for pristine UiO-66 MOF in scientific literature, confirming the successful synthesis of the material [177–181].

In contrast, the XRD pattern of the B,N-CD@UiO-66 nanocomposite preserved the characteristic diffraction peaks of the UiO-66 MOF, including those corresponding to the (111), (200), (220), and (600) planes, thereby confirming that the UiO-66 MOF framework remained intact. While the broad diffraction features typically observed at approximately 10.44˚ and 21.53˚ for B,N-CD were either obscured by the background noise or displayed diminished intensity, this is likely due to the dominance of the crystalline UiO-66 MOF peaks. A slight reduction in the intensity of some UiO-66 peaks, such as the (111) peak, was noted, potentially suggesting partial interactions or binding between the B,N-CD and the MOF framework. Supporting this interaction, the calculated crystallinity percentage decreased to 81.6%, and the crystallite size increased to 96.9 nm. The absence of any new diffraction peaks in the composite pattern indicated that the nanocomposite's formation did not result in a new crystalline phase but rather a successful integration of the B,N-CD within the existing UiO-66 MOF structure.

4.3.2 Fourier Transform Infrared Spectroscopy (FTIR)

As illustrated in figure 15, the B,N-CD spectrum revealed characteristic vibrational peaks of carbon-based materials. A broad absorption band appearing between 3300-3500 cm^{-1} is attributed to the stretching vibrations of O-H groups, likely from hydroxyl functionalities or adsorbed water. Peaks observed in the range of 1380-1600 cm^{-1} correspond to C=C and C=O stretching vibrations in aromatic rings and carbonyl groups, respectively, indicating the presence of graphitic structures within the CD.

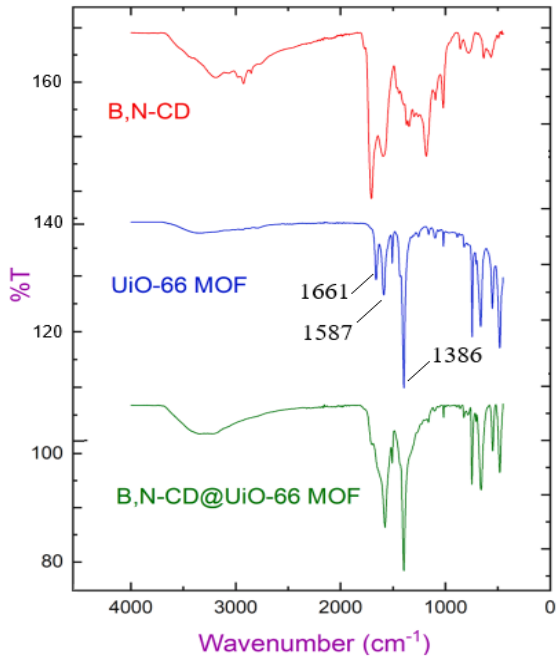

Figure 15: FTIR spectra of UiO-66, B,N-CD, and B,N-CD@UiO-66

The UiO-66 MOF spectrum displayed distinct peaks associated with its terephthalic acid linker. A prominent absorption at 1661 cm^{-1} corresponds to the carboxylate group (COO-) stretching vibration. Peaks at 1587 cm^{-1} and 1386 cm^{-1} are assigned to C=C stretching and bending vibrations within the aromatic ring of the terephthalic acid linker. The sharp peak at 744 cm^{-1} is characteristic of the out-of-plane C-H bending vibration of the benzene ring. Furthermore, peaks in the 450-800 cm^{-1} region are attributed to Zr-O vibrations within the metal-organic framework [182].

The spectrum of the B,N-CD@UiO-66 nanocomposite presented a combination of the peaks observed in the individual B,N-CD and UiO-66 MOF spectra, confirming the successful formation of the nanocomposite. Small shifts in peak positions and variations in peak intensities were noted in the composite spectrum when compared to the individual components, suggesting potential interactions between the B,N-CD and the UiO-66 MOF. Notably, a broadening of the O-H stretching peak in the nanocomposite spectrum could indicate hydrogen bonding interactions between the B,N-CD and UiO-66 MOF. Additionally, an increase in intensity and broadening of the peak at 1587 cm^{-1} in the nanocomposite might be due to new bond formations between the B,N-CD and UiO-66 MOF. Overall, the FTIR analysis offered valuable insights into the functional groups present in each constituent and their potential interactions within the B,N-CD@UiO-66 nanocomposite [182].

4.3.3 X-ray Photoelectron Spectra (XPS)

According to the peaks represented in Figure 16, the presence of B1s and N1s peaks specifically indicated the successful incorporation of boron and nitrogen into the carbon dot structure.

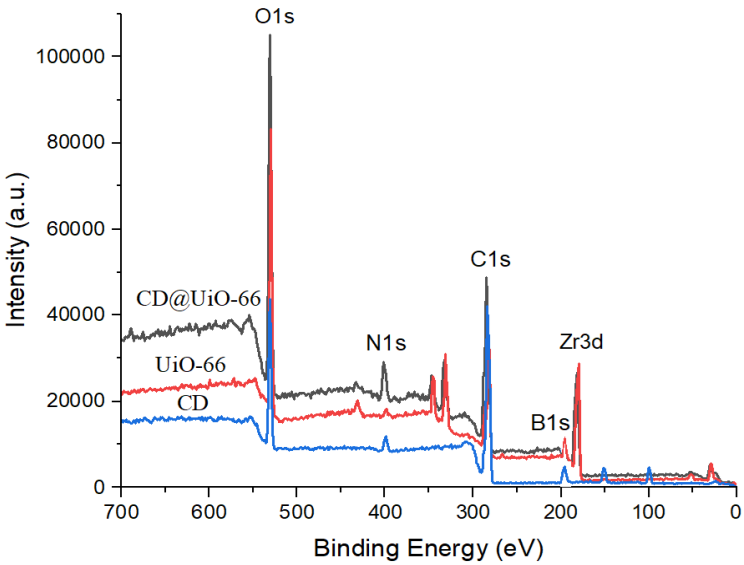

Figure 16: Full XPS scan of synthesized materials

The observation of B-N and C-N bonds highlights an enhanced surface functionalization, which likely improves the dispersibility of the carbon dots and their interaction with the UiO-66 framework. The Zr3d peaks, characteristic of UiO-66 structures, verified the effective integration of the carbon dots with the MOF. Furthermore, the O1s peak provided additional evidence of the UiO-66 framework, with potential contributions from oxygen-containing functional groups present in the B,N-CD.

Detailed analysis of the Zr3d peak (Figure 17a) revealed two deconvoluted peaks at 180.6 eV and 184.5 eV, corresponding to the $Zr3d_{5/2}$ and $Zr3d_{3/2}$ spin-orbit splitting, respectively. This confirms the presence of zirconium within the UiO-66 framework [113,182]. The observed splitting energy of approximately 3.9 eV is a known characteristic feature of Zr [183]. These binding energies are typical for Zr (IV) in the Zr-O bonds found within the UiO-66 MOF structure [183,184].

The deconvoluted C1s spectrum (Figure 17b) showed various carbon bonding environments, which are characteristic of doped carbon materials and composites [170,185]. A peak at approximately 282.6 eV corresponds to graphitic or sp^2-hybridized carbon (C=C), representing the primary carbon backbone structure of the carbon dots or the UiO-66 framework. The peak at around 284.7 eV is attributed to C-N bond, indicating successful nitrogen doping and the incorporation of nitrogen atoms into the carbon lattice. Additionally, a peak at approximately 288.5 eV corresponds to O=C–O or carbonyl (C=O) environment, common in surface functional groups that facilitate interactions between the carbon dots and the UiO-66 framework. These findings collectively confirm the successful nitrogen doping of the carbon dots and

their effective integration into the UiO-66 framework, potentially enhancing functionality and expanding potential applications.

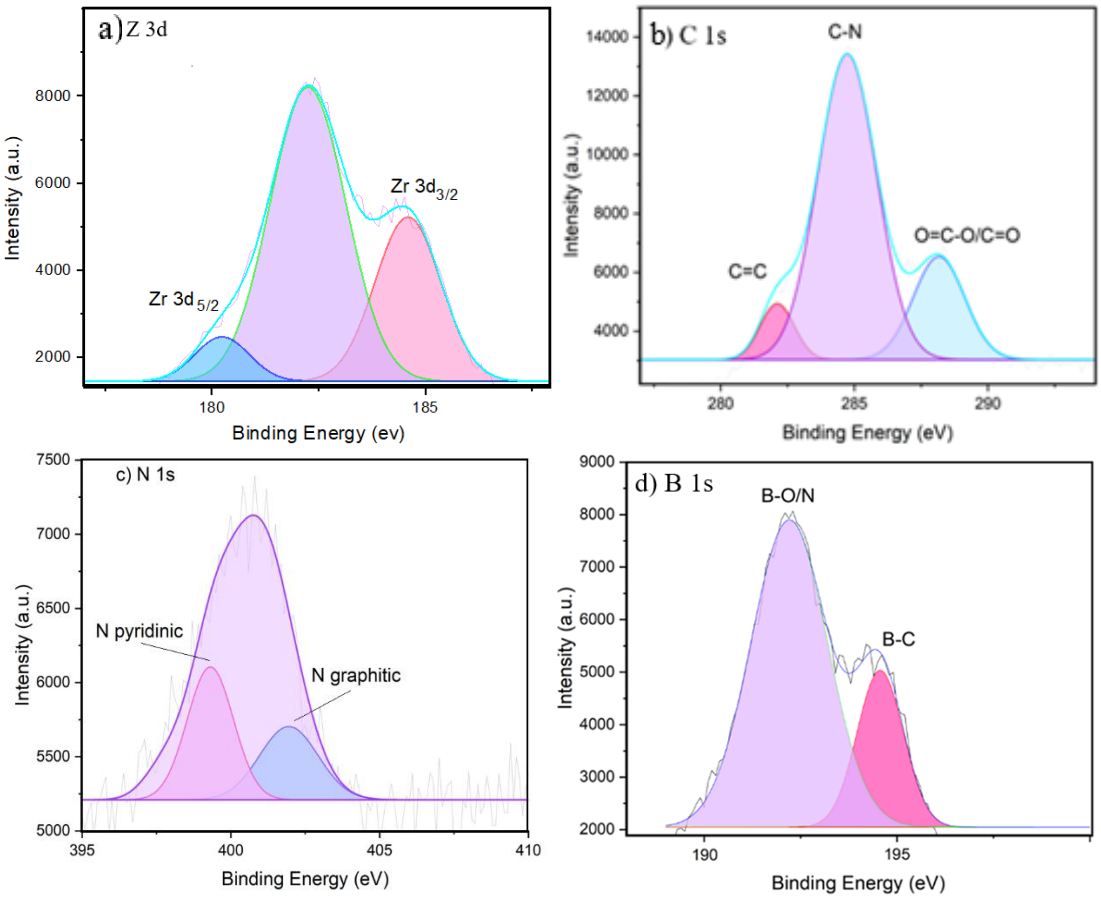

Figure 17: Deconvoluted spectra of B,N-CD@UiO-66 composite (a) Zr3d, (b) C1s (c) N1s and (d) B1s

The N1s spectrum (Figure 17c) was deconvoluted into two main peaks, signifying distinct nitrogen chemical environments. The peak at 399 eV is attributed to pyridinic nitrogen, where nitrogen is bonded to two sp^2-hybridized carbon atoms within a hexagonal carbon framework. In contrast, the peak at 401 eV corresponds to graphitic nitrogen, confirming the incorporation of graphitic nitrogen into the structure of the B,N-doped carbon dots [186,187].

The deconvoluted B1s spectrum revealed two prominent peaks (Figure 17d). The peak at 192.2 eV corresponds to B–O/N. Conversely, the peak at 194.6 eV is attributed to B-C within a sp^2-hybridized environment, indicating that boron atoms have been incorporated into the carbon lattice by substituting carbon atoms and becoming part of the graphene-like structure. The integration of boron, particularly B-C, is crucial for enhancing the electronic properties of the carbon dots by introducing defects and modulating their electronic structure. Finally, a prominent O1s peak at around 530 eV was observed, primarily attributed to oxygen originating from both the UiO-66 framework and oxygen-containing functional groups within the B,N-CD.

In summary, the combined FTIR, EDS and XPS analyses unequivocally confirmed the successful synthesis of the B,N-CD@UiO-66 nanocomposite and verified the presence of all expected key elements within the material.

4.3.4 Nuclear Magnetic Resonance (^{1}H and ^{13}C NMR)

The ^{1}H NMR spectra of the B,N-CD and the B,N-CD@UiO-66 nanocomposite (Figure18) provided critical information regarding their structural compositions and the effect of UiO-66 integration. The B,N-CD spectrum, recorded in DMSO-d_6 at 400 MHz, displayed multiple peaks, indicative of a diverse range of functional groups. The aromatic region, observed between δ 7.87-7.20 ppm, confirmed the presence of aromatic rings, likely resulting from partial graphitization. Signals appearing at δ 6.14-6.05 ppm suggested olefinic or pyrrolic protons, indicating the incorporation of heteroatoms [188]. Oxygenated functional groups, such as hydroxyl, carboxyl, and esters, were evident from signals in the δ 4.06-3.93 ppm range [189]. Furthermore, aliphatic protons (CH, CH_2, CH_3) were observed between δ 3.00-1.09 ppm, consistent with surface modifications. A distinct peak at δ 10.00 ppm suggested the presence of

amine (-NH) or amide (-CONH) groups, directly indicating nitrogen doping, which is vital for enhancing the material's electronic and optical properties.

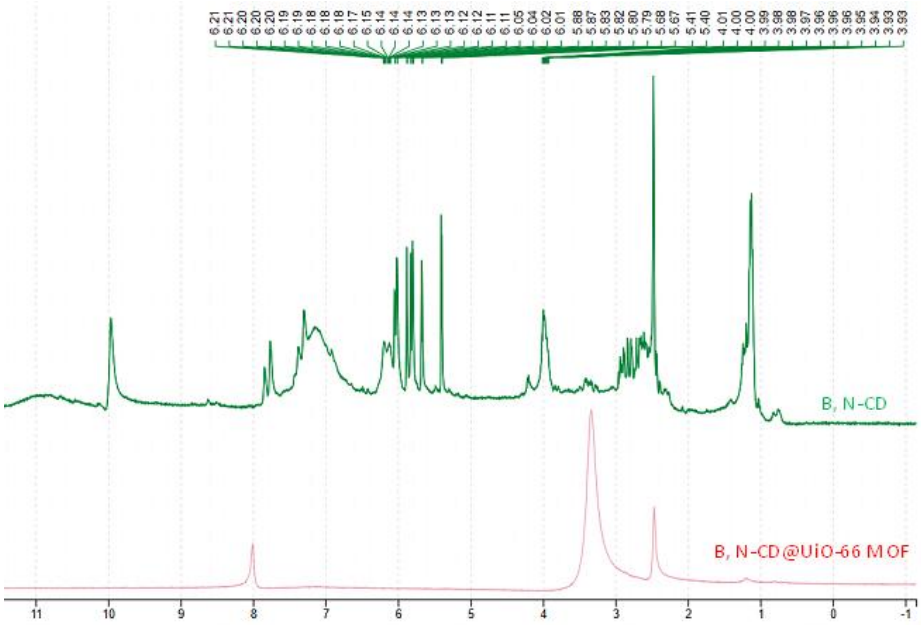

Figure 18: ^{1}H-NMR spectra of B,N-CD and B,N-CD@UiO-66 MOF

Additionally, the ^{1}H NMR spectrum of the B,N-CD@UiO-66 nanocomposite exhibited a simplified spectral profile as illustrated in Figure 18, which suggests significant interactions between the B,N-CD and the UiO-66 framework. The prominent aromatic proton signal at δ 8.03 ppm, characteristic of the BDC linker of UiO-66, confirmed the preservation of the MOF structure [190]. A singlet peak at δ 3.58 ppm corresponded to hydroxyl or amine groups, potentially originating from either the B,N-CD or from interactions within the UiO-66. A minor peak at δ 1.24 ppm indicated residual aliphatic protons. Notably, many of the characteristic signals of the B,N-CD either disappeared or broadened significantly in the composite spectrum, implying restricted molecular motion and host-guest interactions within the MOF. The presence of DMSO (δ 2.50 ppm) and residual water (δ 3.38 ppm) was also observed. Overall, the ^{1}H NMR analysis confirms the successful integration of B,N-CD into

UiO-66 through an *in-situ* approach, resulting in a stable nanocomposite with discernible structural modifications.

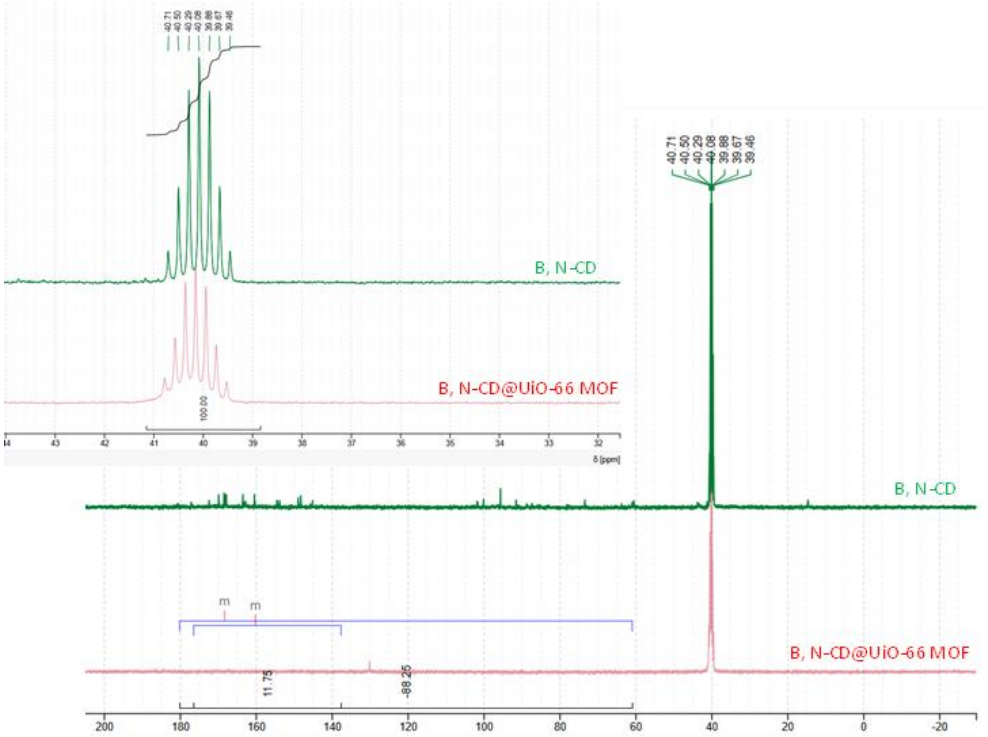

Figure 19: ^{13}C-NMR spectra of B,N-CD and B,N-CD@UiO-66 MOF

The ^{13}C NMR spectra of both the B,N-CD and the B,N-CD@UiO-66 MOF nanocomposite (Figure 19) provided valuable insights into their structural characteristics and the impact of UiO-66 integration. The B,N-CD spectrum exhibited multiple peaks in the δ 160-170 ppm range, which are assigned to sp^2-hybridized carbonyl and conjugated aromatic carbons. These signals are indicative of heteroatom doping with boron and nitrogen. Peaks at δ 101-102 ppm suggested the presence of graphitic carbon structures, while resonances around δ 40-41 ppm and δ 39-40 ppm corresponded to sp^3 carbon centers, likely associated with functional groups linked to nitrogen or boron. Additionally, a peak at δ 14.59 ppm indicated the presence of terminal methyl groups. An observed JJJ-coupling of 21.0 Hz suggested specific carbon-boron interactions within the structure.

In contrast, the B,N-CD@UiO-66 MOF spectrum displayed significant spectral simplification. The absence or weakening of peaks in the δ 160-170 ppm region suggests strong interaction between the B,N-CD and the UiO-66 framework, possibly through coordination or π-π interactions. The dominant peaks around δ 40.15-40.08 ppm correspond to carbon environments within the UiO-66 linker and also to functionalized sp3 carbons from the B,N-CD. A minor peak at approximately 129 ppm hinted at residual aromatic carbon environments derived from the MOF linkers or retained graphitic domains. These observed spectral changes collectively confirm the successful integration of B,N-CD within UiO-66, highlighting strong interactions between the carbon dots and the MOF structure, and thereby validating the effectiveness of the in-situ synthesis approach in forming a well-integrated hybrid material.

4.4 Optical Characterization

4.4.1 Photoluminescence Spectroscopy (PL)

Figure 20 presents the photoluminescence spectra of synthesized products, providing insights into their optical properties. The B,N-CD exhibited a strong emission peak centered at 440 nm, which is characteristic of carbon dots [191]. This observed blue emission is primarily attributed to the radiative recombination of electron-hole pairs within the sp^2-hybridized carbon domains. This phenomenon is further influenced by surface states and structural defects introduced by the nitrogen and boron doping.

The PL spectrum of UiO-66 displayed a broader emission profile spanning the range of 32-600 nm. This broad emission is attributed to its MOF structure, specifically involving ligand-to-metal charge transfer (LMCT) processes or interactions between the Zr-based nodes and the organic linkers. A red shift to 456 nm relative to the B,N-

CD's emission indicates distinct optical properties and electronic structures for the UiO-66 MOF.

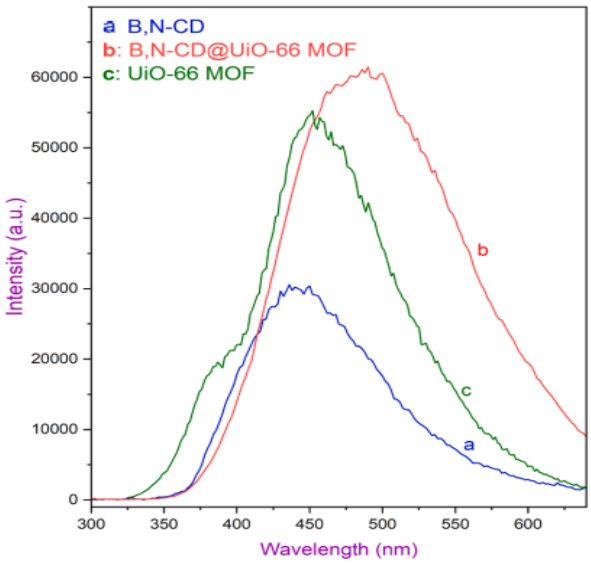

Figure 20: PL intensity of UiO-66, B,N-CD and B,N-CD@UiO-66 composite

The B,N-CD@UiO-66 nanocomposite's PL spectrum incorporated features from both the B,N-CD and UiO-66 components. Notably, the nanocomposite exhibited a significant enhancement in PL intensity compared to its individual constituents. The emission spectrum revealed a broad peak in the blue-green region, which was red-shifted to 486 nm. This spectral shift suggests strong electronic interactions or energy transfer mechanisms between the B,N-CD and the UiO-66 framework.

Upon integration into UiO-66, the B,N-CD may experience enhanced π-π stacking interactions or electronic coupling with the MOF framework. Such interactions can extend electron delocalization, consequently reducing the energy gap between excited and ground states, which ultimately leads to the observed fluorescence red shift. Furthermore, potential charge transfer mechanisms between the B,N-CD and UiO-66 could also contribute to this shift by modifying the electronic structure of the

nanocomposite. This overall enhancement in PL is attributed to synergistic effects, including energy transfer and improved charge separation, which are facilitated by the interface created between the two components. The pronounced red shift in emission strongly suggests the involvement of Förster resonance energy transfer (FRET) or similar mechanisms. This reflects modifications in the electronic states of the B,N-CD resulting from their integration within the UiO-66 matrix. These changes likely stem from enhanced coupling between the electronic states of the carbon dots and the MOF, leading to an optimized optical response. The increased fluorescence intensity and the observed spectral shifts highlight the promising potential of the B,N-CD@UiO-66 nanocomposite for fluorescence-based applications, offering improved sensitivity and selectivity for target analytes.

4.4.2 UV-Vis Spectroscopy

The UV-Vis absorption and emission characteristics of the synthesized materials illustrated in Figure 21. The UiO-66 absorption spectrum displayed typical UV region peaks, attributed to ligand-to-metal charge transfer (LMCT) transitions. In contrast, the B,N-CD spectrum showed broad absorption across the UV-visible range, characteristic of carbon dots. This broadness results from π-π^* transitions within sp^2-hybridized domains and n-π^* transitions from surface functional groups.

The B,N-CD@UiO-66 nanocomposite absorption spectrum combined features from both UiO-66 and B,N-CD, confirming the successful incorporation of B,N-CD into the MOF. Its broad absorption spectrum suggests enhanced light-harvesting capabilities, making it beneficial for fluorescence-based sensing. While the individual UiO-66 and B,N-CD emission spectra weren't analyzed (as they weren't directly relevant to the sensing application), the B,N-CD@UiO-66 nanocomposite exhibited excitation

wavelength-dependent fluorescence (EWD). Its emission peak shifted from 455 nm to 430 nm as the excitation wavelength increased from 250 nm to 330 nm. This behavior points to multiple emissive centers within the nanocomposite [192–194]. Interactions between the B,N-CD and UiO-66 framework may have created new emissive states or altered B,N-CD's energy levels, leading to this EWD.

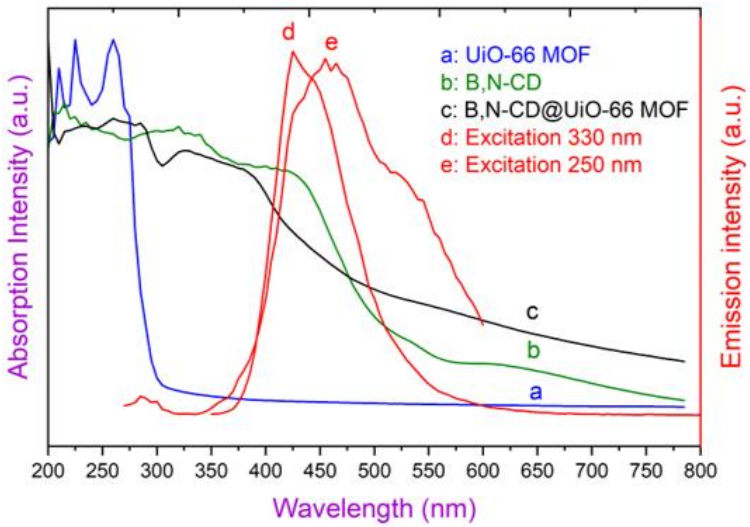

Figure 21: UV-vis absorption and emission spectra of UiO-66, B,N-CDs, and B,N-CD@UiO-66 composite

Additionally, the UiO-66 MOF might stabilize specific B,N-CD emissive states, influencing the emission shift. This EWD suggests the nanocomposite's fluorescence response to cefixime could be modulated by excitation wavelength, possibly through excitation-dependent charge or energy transfer mechanisms. These mechanisms might stem from selective interactions between cefixime, and the nanocomposite's surface groups, boosting sensing capabilities [192,193]. This emission tunability offers flexibility in optimizing detection conditions for cefixime. Subsequent investigations confirmed that varying the excitation wavelength from 330 nm to 400 nm did not significantly alter the maximum emission peak, which consistently remained at

430 nm. Therefore, all further studies were conducted using a 330 nm excitation wavelength.

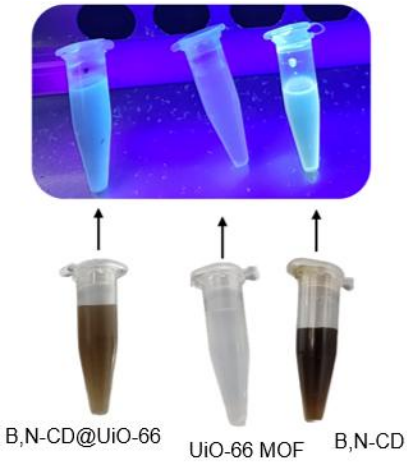

Figure 22: Synthesized materials under UV and natural light

Figure 22 illustrates the visual observations of the samples under natural and UV light. The B,N-CD offered a strong whitish-blue fluorescence under UV irradiation typical of carbon dots, due to quantum confinement effects and emissive surface state interactions. The UiO-66 MOF exhibited weak blue or pale violet fluorescence under UV excitation. The B,N-CD@UiO-66 nanocomposite however, displayed significantly brighter blue fluorescence with a subtle cyan shift compared to individual components.

4.5 Assessment of Quantum Yield in Aqueous Solution

We determined the quantum yields (Φ) of our synthesized samples using a comparative method, following established procedures [195]. Rhodamine B (RhB), with a known quantum yield of 0.65 in ethanol, served as our standard. To minimize potential re-absorption and inner filter effects, we ensured that the absorbance of all samples remained below 0.10. The quantum yield was calculated using the following equation:

$$\Phi_{sample} = \phi_{ref} \times \left(\frac{I_{sample}}{I_{ref}}\right) \times \left(\frac{A_{ref}}{A_{sample}}\right) \times \left(\frac{n^2 sample}{n^2 ref}\right)$$

Where Φ_{sample} and Φ_{ref} represent the quantum yields of the sample and reference, respectively, I_{sample} and I_{ref} are the integrated fluorescence intensities of the sample and reference, A_{sample} and A_{ref} are the absorbance values at the excitation wavelength, and n_{sample} and n_{ref} are the refractive indices of the solvents utilized. The refractive index correction factor was effectively 1, as the refractive indices of the sample and reference solvents were considered equal (n_{sample}= n_{ref} =1.361).

The B,N-CD@UiO-66 nanocomposite displayed a quantum yield of 32.9%, which indicates a reduction in fluorescence efficiency when compared to the B,N-CD alone. This decreased performance likely stems from surface passivation effects that occur during integration with UiO-66, potentially altering the electronic states of the B,N-CD and subsequently diminishing their quantum yield.

4.6 Assessment of Stability in Aqueous Solution

To assess the sensor's suitability for extended use in sensing, the optical stability of the B,N-CD@UiO-66 nanocomposite in aqueous solution was evaluated over 27 days, under both room temperature and refrigerated conditions (12°C). As depicted in Figures 23a-b, the initial fluorescence intensity was highest on the first day for both storage methods.

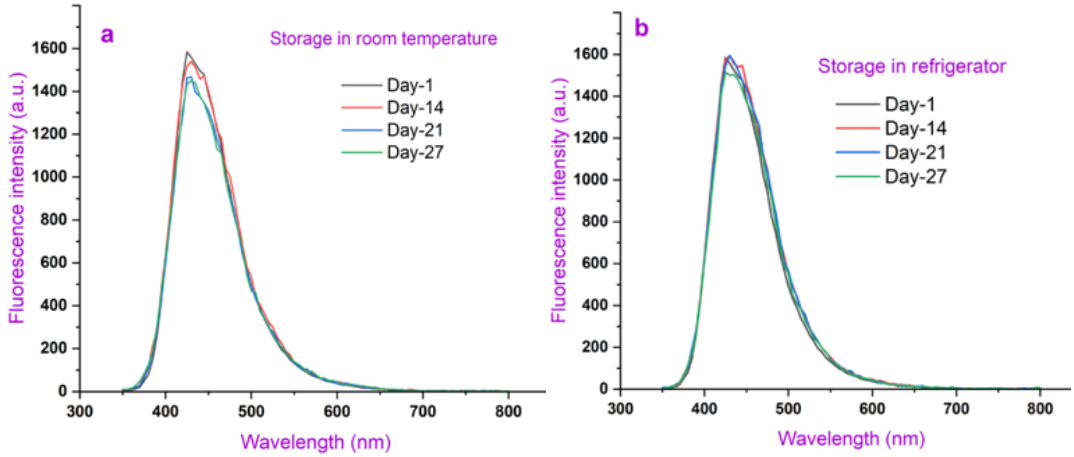

Figure 23: Fluorescence intensity of B,N-CD@UiO-66 over 27 days without pH adjustment in (a) room temperature and (b) refrigerator

A gradual decline in fluorescence intensity was observed across the 27-day period under both conditions. Specifically, fluorescence intensity dropped by 4.12% at room temperature and by 2.23% at 12°C over this period (Figure 24).

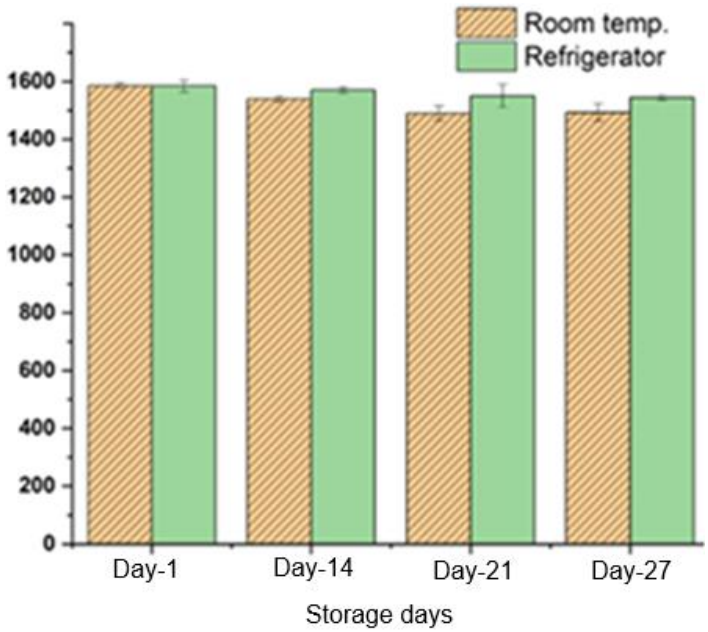

Figure 24: Stability of B,N-CD@UiO-66 stored for 27 days without pH adjustment in room temperature and refrigerator

Despite this minor reduction, the nanocomposite largely maintained its initial fluorescence. These findings demonstrate the B,N-CD@UiO-66 nanocomposite's reasonable optical stability over time, particularly when refrigerated, suggesting its promise for long-term fluorescence-based sensing applications, such as detecting antibiotics like cefixime. These results align with earlier research, including the study by Qin et al. [196], which observed only a minor reduction in the fluorescence intensity of Cd-MOF/Tb^{3+} nanosheets after being dispersed in deionized water for seven weeks.

To further validate the long-term reliability of nanocomposite, an extended 60-day trial revealed only a 2.5% decrease in fluorescence intensity. This level of stability often surpasses that reported in the literature, where fluorescence-based sensors are typically tested for just two weeks in aqueous solutions. Additionally, the solid-state B,N-CD@UiO-66 nanocomposite, when stored for over six months, retained 100% of its fluorescence performance, underscoring its exceptional robustness. These collective results confirm the B,N-CD@UiO-66 nanocomposite's high stability and suitability for practical sensor applications.

4.7 Effect of pH

The nanocomposite displayed pH-dependent fluorescence, reaching its maximum intensity at pH 5.12, indicating optimal optical performance in slightly acidic conditions (Figure 25). Fluorescence intensity was lowest at pH 2.9, likely because of protonation of functional groups on both the B,N-CD and the UiO-66 framework under strong acidic conditions. This protonation can lead to non-radiative energy dissipation pathways or disrupt energy transfer between the B,N-CD and UiO-66, resulting in fluorescence quenching.

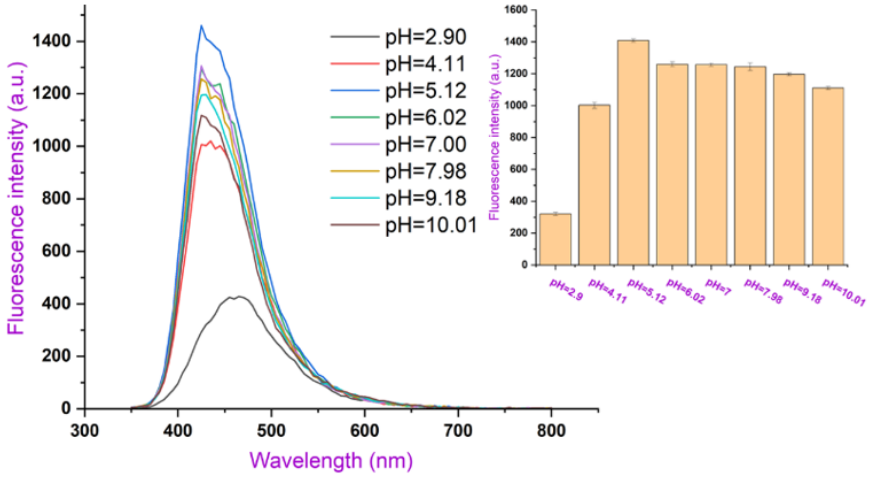

Figure 25: Influence of pH variation on fluorescence intensity of B,N-CD@UiO-66

As the pH increased from 2.9 to 6.02, a significant rise in fluorescence intensity occurred, peaking at pH 5.12. However, further increasing the pH from 6.02 to 7.98 led to a slight decrease in fluorescence, suggesting that a near-neutral pH environment is less favorable for fluorescence compared to the slightly acidic conditions. This reduction might be attributed to deprotonation effects that alter the electronic states and energy transfer efficiency within the nanocomposite. At pH 9.18-10, fluorescence intensity continued to decrease, potentially due to further deprotonation of surface groups, which could lead to aggregation or destabilization of the composite structure. Based on the findings, pH 5.12 was chosen as the optimal pH for sensing experiments, considering the nanocomposite's stability and its highest fluorescence intensity.

4.8 Florescence-based Sensing Experiments

4.8.1 Determination of Linear Range, LOD and Calibration Curve

The fluorescence quenching of the B,N-CD@UiO-66 nanocomposite by Cefixime (CFX) was investigated across two concentration ranges: 0-100 nM and 0-20 µM. As depicted in Figure 26a, a gradual decrease in fluorescence intensity was observed with increasing CFX concentration in both ranges, indicating an interaction between CFX and the nanocomposite.

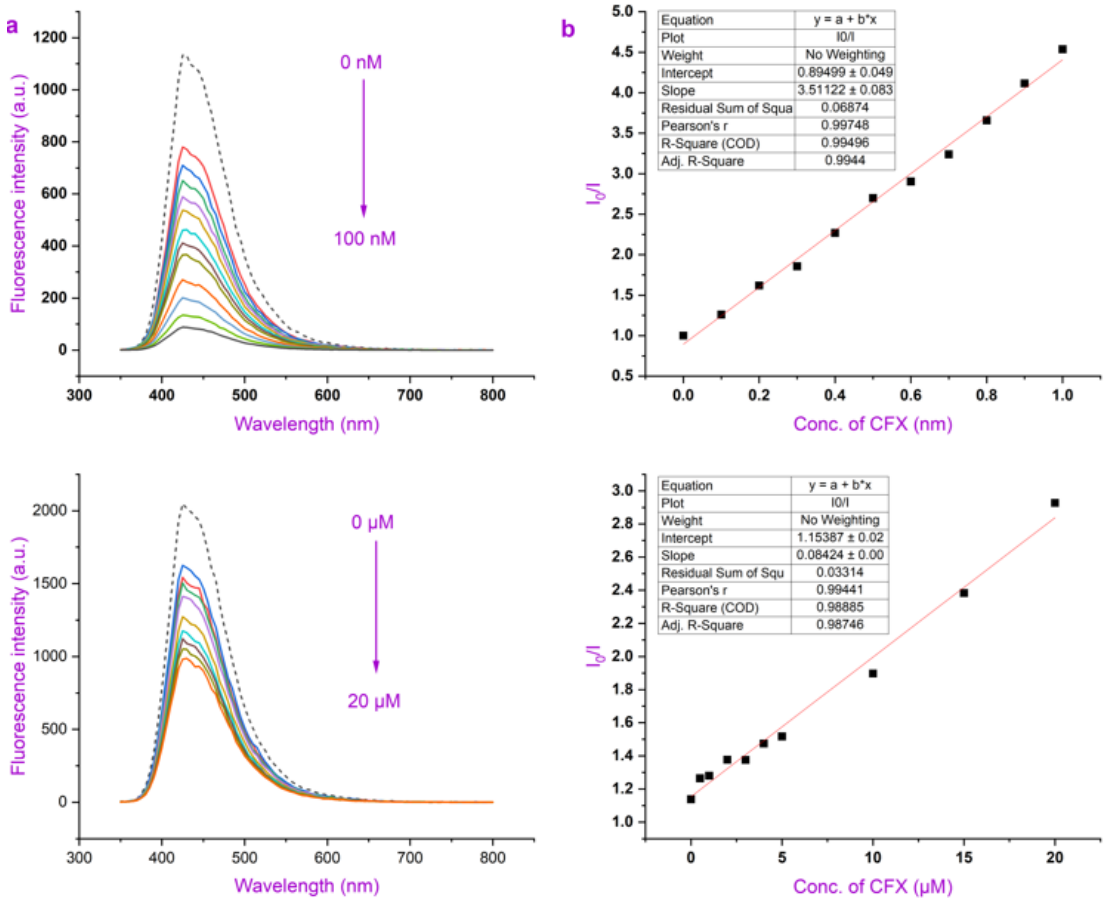

Figure 26: (a) Fluorescence intensity of the B,N-CD@UiO-66 composite as a function of increasing cefixime concentration and (b) Stern-Volmer plot

This quenching behavior suggests potential energy transfer or charge transfer processes, or interactions between CFX functional groups (e.g., amino or carboxyl) and the nanocomposite's surface functionalities (e.g., boronic acid or amine groups). More pronounced quenching was noted at lower CFX concentrations. To quantify the quenching efficiency, the Stern-Volmer equation was applied [197,198]:

$$\frac{I_0}{I} = K_{SV}[Q] + 1$$

where I_0 and I are the fluorescence intensities without and with CFX, respectively; KSV is the Stern-Volmer quenching constant; and [Q] is the CFX concentration. The Stern-Volmer plots exhibited good linearity in both ranges, with R^2 values of 0.995 for 0-100 nM (Figure 26b) and 0.989 for 0-20 µM. The calculated K_{SV} values were

3.51 M^{-1} for the lower concentration range and 0.0842 M^{-1} for the higher range. The limit of detection (LOD), calculated as $3\sigma/K_{SV}$ (σ being the standard deviation of blank measurements), was determined to be 4.21 nM (1.907 ng/mL) for the lower concentration range and 17.5 nM for the higher range. These LODs highlight the exceptional sensitivity of the B,N-CD@UiO-66 nanocomposite for CFX detection, with limits significantly below regulatory maximum allowable concentrations for pharmaceuticals set by bodies like the EU and WHO. Compared to previously reported methods for CFX detection (Table 1), the B,N-CD@UiO-66 nanocomposite-based sensor demonstrated a lower LOD and a relatively wider linear range, indicating improved sensitivity and a broader analytical window [196,199–202].

Table 1: Comparative performance of fluorescent materials for CFX sensing

Fluorescent sensors	Linear range (μM)	LOD (nM)	Refs.
B,N-CD@UiO-66	0–0.1 0–20	4.21 17.5	This study
WS_2 QDs/fluorescein	0.441–5.513	99.2	[203]
Tb-MOF	0.1–150	31.6	[204]
Zn-PDC-Tb^{3+}	0–10	140	[205]
Cd-MOF-Tb^{3+} nanosheets	0–6.0	26.7	[206]
Fluorescent carbon dots	0.2–8 μM	50.0	[207]

Further analysis suggests the quenching mechanism is predominantly static, supported by the unchanging emission peak position of the nanocomposite upon CFX addition. Static quenching typically involves the formation of a non-fluorescent ground-state complex between the fluorophore and quencher, leaving the emission wavelength of unquenched fluorophores unaffected. At higher CFX concentrations, a slight deviation from linearity in the Stern-Volmer plot was observed.

This deviation points to the contribution of additional quenching mechanisms, such as inner filter effects (absorption of excitation or emission light by the quencher) or secondary quenching processes (e.g., energy transfer between excited quencher molecules). To further elucidate the quenching mechanism, UV-vis absorption spectra, fluorescence spectra, and fluorescence lifetime measurements were conducted, with results discussed in subsequent sections.

4.9 The Sensing Properties of B,N-CD@UiO-66 Nanocomposite

The selectivity and anti-interference ability of the B,N-CD@UiO-66 nanocomposite-based fluorescence sensor were thoroughly evaluated by testing its response to Cefixime (CFX) in the presence of various interfering substances, including other antibiotics and metal ions.

4.9.1 Fluorescence Sensing of Antibiotics

Figure 27 displays the fluorescence spectra of the nanocomposite when exposed to CFX alongside various interfering antibiotics: Amoxicillin (Amox), Tetracycline (Tet), Metronidazole (Metro), Ciprofloxacin (Cip), and Cefuroxime (Cefr).

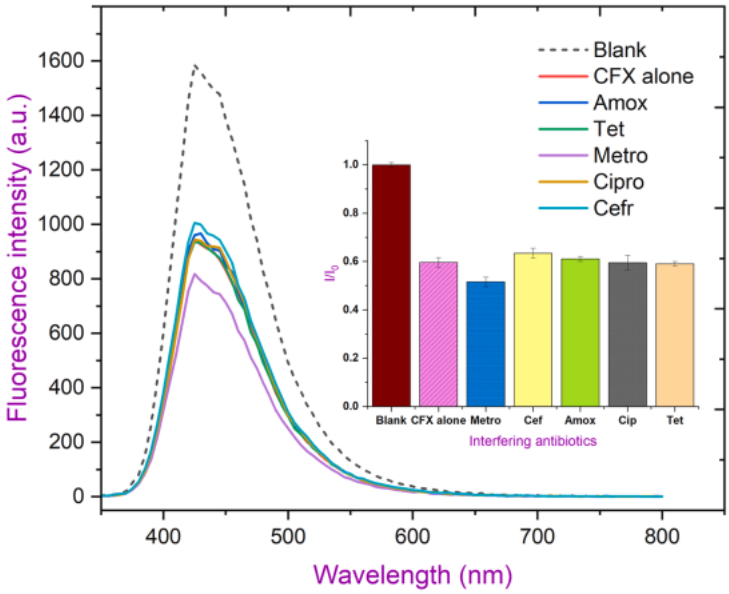

Figure 27: Fluorescence quenching of B,N-CD@UiO-66 upon the addition of CFX and interfering antibiotics

The introduction of CFX alone led to significant fluorescence quenching. While other antibiotics also caused some degree of quenching, Metronidazole (Metro) showed the most pronounced quenching effect, suggesting a stronger interaction with the synthesized nanocomposite. This is likely due to the electron-withdrawing nitro group in Metro's structure, which enhances electronic interactions with the fluorophore's excited states, promoting non-radiative decay and greater quenching [208]. Additionally, Metro's smaller, more planar structure allows for more efficient access and interaction within the porous framework compared to bulkier cephalosporins like CFX and Cefr.

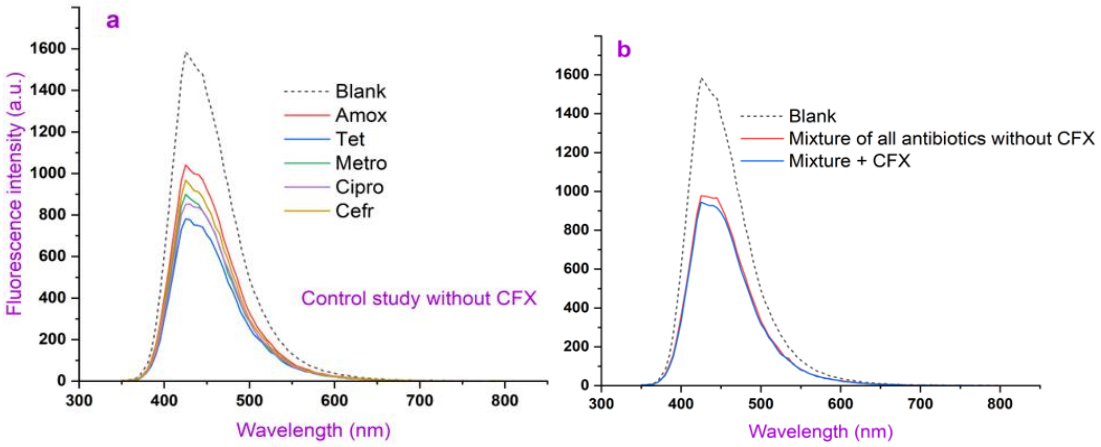

Figure 28: (a) Fluorescence quenching of interfering antibiotics without CFX and (b) equimolar mixture of all studied antibiotics with CFX

Control experiments with individual antibiotics in the absence of CFX (Figure 28a) revealed that Metro alone caused slightly higher fluorescence intensity than when both Metro and CFX were present. This indicates that CFX might partially displace Metro from binding sites on the nanocomposite when both are present. Since Metro is a more effective quencher, this displacement would lead to less overall quenching compared to Metro acting alone. Despite the presence of these interfering antibiotics, both

individually and in a mixture (Figure 28b), the B,N-CD@UiO-66 nanocomposite demonstrated minimal interference in CFX detection, confirming good selectivity.

4.9.2 Fluorescence Sensing of Metal Ions

Figure 29 illustrates the impact of various interfering metal ions (Ag^{+}, Ni^{2+}, Fe^{2+}, K^{+}, Cu^{2+}, Mn^{2+}, Mg^{2+}, Ca^{2+}, and Fe^{3+}) on the fluorescence detection of CFX by the nanocomposite. The addition of CFX alone resulted in the most significant fluorescence quenching, indicating a strong and specific interaction. This is likely attributed to the reactive β-lactam ring in CFX and potential hydrogen bonding and electrostatic interactions between CFX's carboxylate (-COO−) and amine ($-NH_2$) groups and the nanocomposite's functional groups.

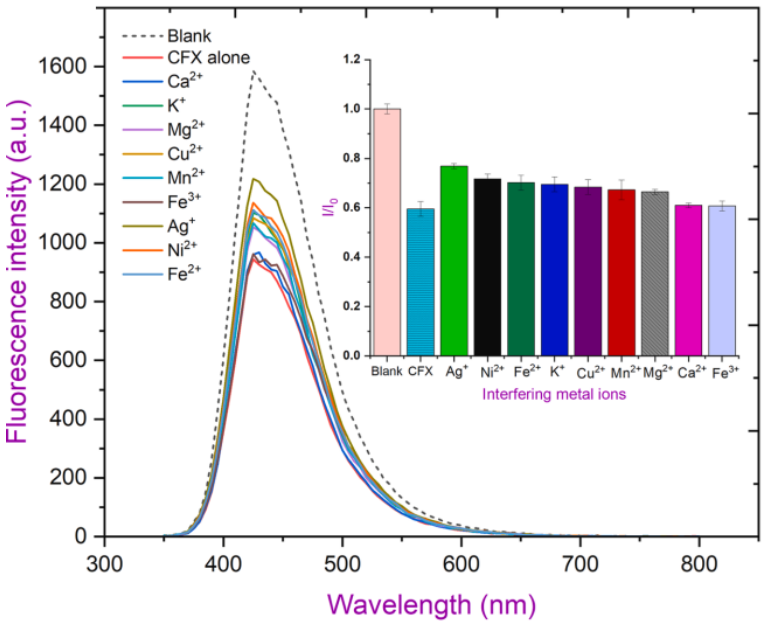

Figure 29: Fluorescence quenching of B,N-CD@UiO-66 upon the addition of CFX and interfering metal ions

While most metal ions caused moderate quenching, Ag^{+} showed the least interference. Redox-active metal ions such as Fe^{3+}, Fe^{2+}, Cu^{2+}, Ni^{2+}, and Mn^{2+} may facilitate non-radiative decay pathways, leading to fluorescence quenching. In contrast, alkali and

alkaline earth metals (K^+, Ca^{2+}, Mg^{2+}) generally exhibited weaker interactions due to their lower coordination affinity.

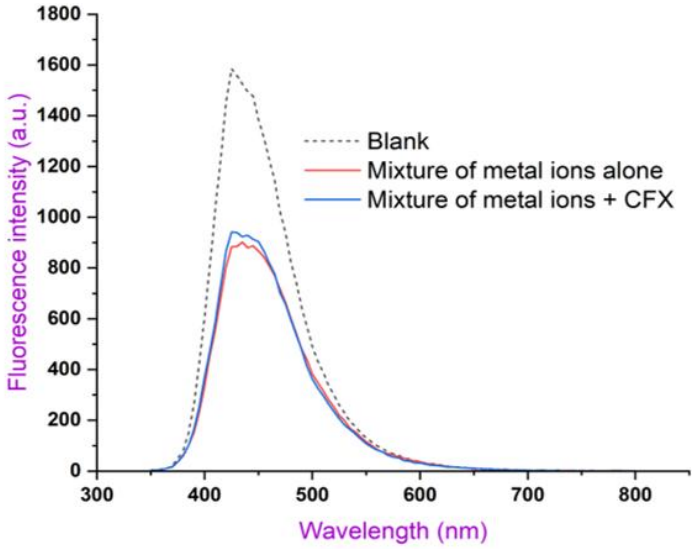

Figure 30: Fluorescence quenching of equimolar mixture of all studied metal ions, both with and without CFX

Control experiments with metal ions alone (Figure 30) showed similar trends, confirming that although metal ions can quench the nanocomposite's fluorescence, they do not significantly impede the selective detection of CFX. This suggests that CFX maintains a strong and preferential binding affinity with the nanocomposite, thereby minimizing the impact of potential metal ion interference.

4.9.3 Effect of Salinity on Sensor

To evaluate how salinity impacts the sensor's performance, the fluorescence response of the B,N-CD@UiO-66 nanocomposite to Cefixime (CFX) was examined across a range of NaCl concentrations (0.1 M to 50 M). As presented in Figure 31, CFX alone caused significant fluorescence quenching. However, the presence of NaCl led to varied changes in fluorescence intensity. At lower NaCl concentrations (0.1 M to 0.5 M), a slight increase in fluorescence intensity was observed compared to the CFX-only condition. This suggests a reduction in the CFX-induced quenching, possibly due

to a shielding effect of NaCl ions on electrostatic interactions between CFX and the nanocomposite (e.g., involving CFX's carboxylate groups and the nanocomposite's functional groups). Conversely, at higher NaCl concentrations (1.0 M to 50 M), a notable decrease in fluorescence intensity was observed. This reduction is likely attributable to the competitive binding of Na^+ and Cl^- ions with either CFX or the nanocomposite within the porous UiO-66 structure, thereby impeding the effective interaction between CFX and the sensing material.

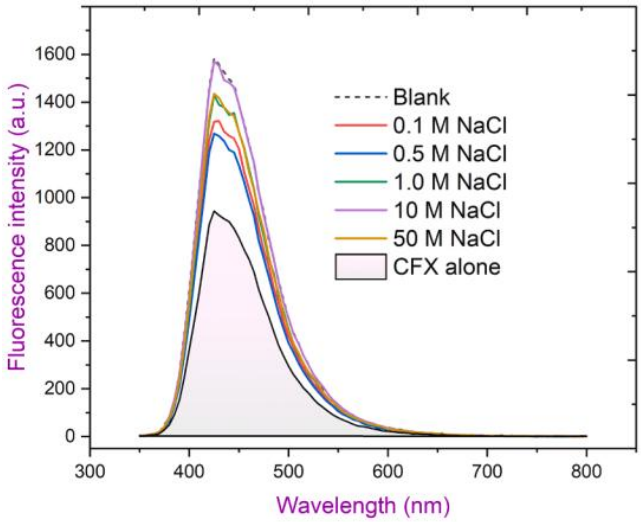

Figure 31: Effect of salinity on Fluorescence performance of B,N-CD@UiO-66

These findings indicate that while the B,N-CD@UiO-66 nanocomposite demonstrates moderate fluorescence quenching in low-salinity environments for CFX, its sensitivity is compromised by high salt concentrations. Future research will explore strategies to improve the sensor's salt tolerance, such as incorporating hydrophobic or salt-resistant functionalities onto the nanocomposite surface.

4.10 Recyclability of the B,N-CD@UiO-66 Nanocomposite Sensor

We assessed the recyclability of the B,N-CD@UiO-66 nanocomposite sensor over five consecutive sensing cycles. After each cycle, we recovered the nanocomposite via centrifugation, washed it with ethanol, and dried it at 70°C before reusing.

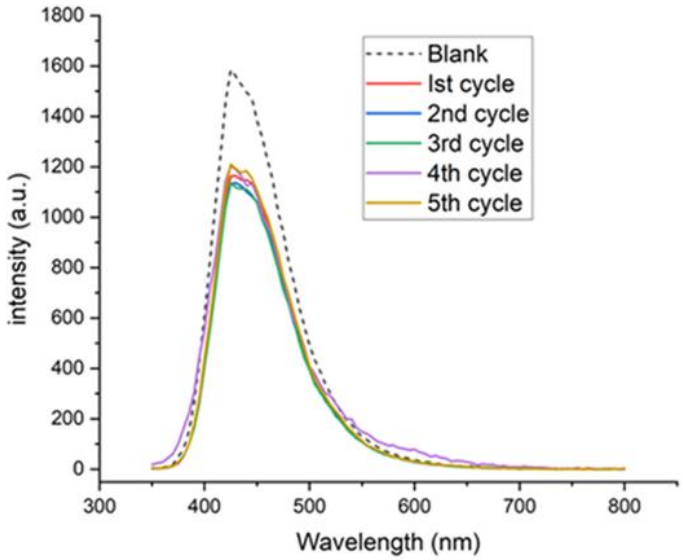

Figure 32: Recycling performance of B,N-CD@UiO-66 composite

As Figure 32 illustrates, we observed a slight improvement in fluorescence quenching during the initial cycles (second and third). This could be due to a subtle rearrangement of the B,N-CD within the UiO-66 framework, potentially making CFX binding sites more accessible. However, subsequent cycles (fourth and fifth) showed a gradual decrease in fluorescence quenching. This decline in sensor performance might stem from several factors, including the adsorption of impurities from the solution during repeated use, which can interfere with fluorescence, or potential degradation or structural changes within either the B,N-CD or the UiO-66 framework itself.

These findings suggest the B,N-CD@UiO-66 nanocomposite offers good reusability for up to three cycles, initially even showing a slight performance boost, before a gradual decline in subsequent uses.

4.11 Sensing of Cefixime in Real Samples

To assess the practical applicability of the newly synthesized B,N-CD@UiO-66 nanocomposite as a fluorescent probe, we spiked real-world samples, specifically honey, tap water, and seawater, with known concentrations of Cefixime (CFX).

Table 2: Analytical results (n = 4) for detection of CFX in real samples

Samples	**Initial (µM)**	**Spiked (µM)**	**Found (µM) [a]**	**n**	**Average Recovery (%)**	**RSD (%)**	**UV-Vis (µM) [b]**
Urine	0.00	0.00	Not detected				
		0.20	0.197	1			
			0.195	2	96.9	1.54	0.199
			0.193	3			
			0.190	4			
Honey	0.00	0.00	Not detected				
		0.20	0.221	1			
			0.197	2	101.63	5.34	0.211
			0.199	3			
			0.198	4			
Tap water	0.00	0.00	Not detected				
		0.20	0.189	1			
			0.198	2	98.0	2.29	0.201
			0.200	3			
			0.197	4			
Seawater	0.00	0.00	Not detected				
		0.20	0.198	1			
			0.198	2	100.85	3.31	0.199
			0.211	3			
			0.196	4			

[a] Fluorescence sensor; [b] UV-vis average result per sample.

The recovery percentage (%) of CFX in each sample matrix and the relative standard deviation (RSD%) were calculated using the following equations to evaluate the accuracy and reliability of the developed sensor:

$$\text{Recovery (\%)} = \frac{found\ CFX}{initial\ CFX + spiked\ CFX} \times 100$$

$$\text{RSD (\%)} = \frac{standard\ deviation}{mean} \times 100$$

Real-world matrices, such as honey and biological fluids, frequently contain proteins and sugars that can interfere with fluorescence-based sensing, either by acting as quenching agents or through other matrix effects, potentially leading to inaccurate CFX quantification. To minimize these interferences, samples in this study underwent pretreatment, including 0.22 μm filtration and dilution, before analysis.

As detailed in Table 2, the developed method demonstrated exceptional accuracy and precision in the analysis of these spiked samples. Recovery rates were found to range from 96.9% to 101.63%, with relative standard deviations (RSDs) between 1.54% and 5.34% (n=4). To further validate the analytical performance, CFX concentrations in the spiked samples were also determined using a standard UV-Vis spectrophotometric method. The results obtained from both methodologies exhibited good agreement, confirming the accuracy and reliability of the B,N-CD@UiO-66 nanocomposite-based fluorescence sensor for the determination of CFX in complex matrices.

4.12 Fluorescence Quenching Mechanism of Sensor

As discussed previously, the emission peak position of the B,N-CD@UiO-66 nanocomposite remained unchanged even after adding CFX.

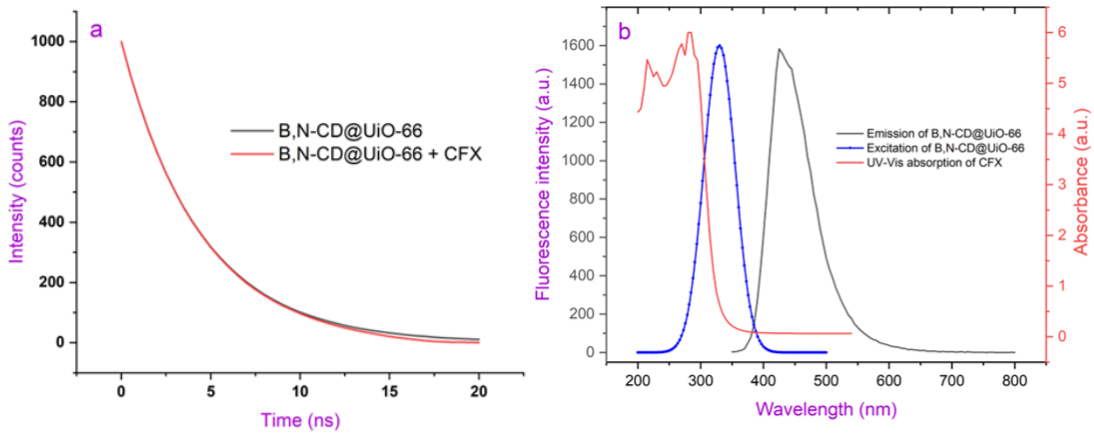

Figure 33: (a) Fluorescence decay curve of B,N-CD@UiO-66 with and without CFX (b) UV-vis adsorption spectrum of CFX and excitation/emission spectrum of B,N-CD@UiO-66

This suggests a static quenching mechanism is at play. Such a mechanism points to the formation of a non-fluorescent ground-state complex between the composite and CFX, likely through weak intermolecular forces like hydrogen bonding or electrostatic interactions. Supporting this, fluorescence lifetime measurements (Figure 33a) showed a negligible change in the average lifetime after CFX addition (from 4.37 ns for the nanocomposite alone to 4.40 ns with CFX), further solidifying the dominance of static quenching [197,198].

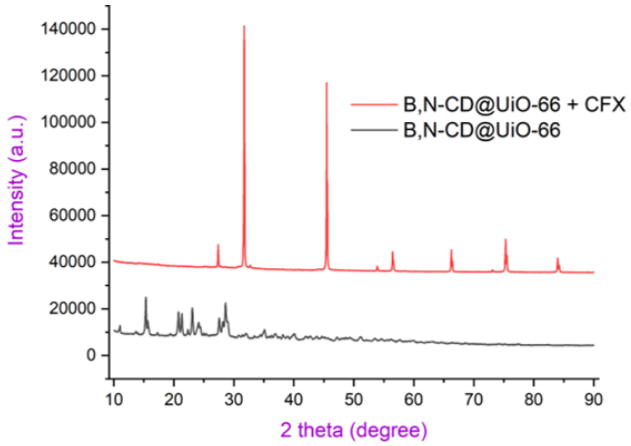

Figure 34: XRD patterns of B,N-CD@UiO-66 and B,N-CD@UiO-66 with CFX

The involvement of Inner Filter Effects (IFE) was also evident [196]. Although the UV-Vis absorption spectrum of CFX shows some overlap with the B,N-CD@UiO-66 nanocomposite's emission spectrum (Figure 33b), this overlap is limited, suggesting IFE isn't the primary quenching mechanism. However, the observed deviation from linearity in the Stern-Volmer plot at higher CFX concentrations still points to some IFE contribution. Yet, the consistent fluorescence lifetime measurements (Figure 32a) reiterate that static quenching plays a more significant role in the overall quenching process. Furthermore, XRD analysis (Figure 34) revealed significant changes in the crystal structure of the B,N-CD@UiO-66 nanocomposite after CFX addition. This provides additional evidence for the formation of a ground-state complex as part of the quenching mechanism. In summary, the fluorescence quenching of B,N-CD@UiO-66 by CFX is primarily due to a combination of static quenching (major contribution) and inner filter effects (minor contribution).

Chapter 5

CONCLUTION AND FUTURE PERSPECTIVES

5.1 Novelty and Significance of the Study

The novelty and significance of this research are rooted in the synergistic combination of advanced nanomaterials and their tailored properties, directly addressing critical limitations in current antibiotic detection methodologies.

5.1.1 Novelty in B,N-Codoped Carbon Dots Synthesis and Properties

The first key novelty lies in the precise synthesis and utilization of Boron and Nitrogen co-doped Carbon Dots. While carbon dots themselves are known luminescent nanomaterials, the strategic co-doping with heteroatoms like B and N offers distinct advantages that are central to this study's innovation:

Enhanced Fluorescence Quantum Yield: The incorporation of N atoms, particularly in configurations like pyridinic-N and pyrrolic-N, creates new electronic states within the CD bandgap, acting as emissive traps. This significantly increases the fluorescence quantum yield compared to undoped or singly doped CDs, leading to brighter and more efficient probes. However, note that the B,N-CD@UiO-66 nanocomposite exhibited a quantum yield of 32.9%, indicating a decrease in fluorescence efficiency compared to the B,N-CDs (67.8%). This reduction is likely due to surface passivation effects during integration with UiO-66, which can change the electronic states of the B,N-CDs and subsequently lower their quantum yield.

Improved Photostability: Both B and N doping contribute to the passivation of surface defects on the CDs, reducing non-radiative recombination pathways. This

results in superior photostability, crucial for sustained fluorescence signal integrity during prolonged analysis and in demanding environmental conditions, overcoming the photobleaching issues often associated with traditional organic dyes. The B,N-CD@UiO-66 nanocomposite demonstrated notable optical stability over time. Its fluorescence intensity decreased by only 4.12% at room temperature and by a mere 2.23% when stored at refrigerator (at 12°C) over a 27-day period. These findings underscore the composite's reasonable long-term optical stability, particularly under refrigerated conditions. This performance is a significant advantage, especially when compared to several other reported fluorescent sensors that typically retain only 50% of their stability within a two-week timeframe. Such robust stability suggests the strong potential of the B,N-CD@UiO-66 nanocomposite for practical, long-term use in fluorescence-based sensing applications, including the reliable detection of antibiotics like cefixime.

Tunable Optical Properties: The electron-donating nature of N and the electron-withdrawing nature of B enable fine-tuning of the electronic band structure of the CDs. This allows for precise control over their absorption and emission wavelengths, offering versatility in designing sensors for various target analytes.

Creation of Active Sites: The heteroatom doping introduces specific functional groups and Lewis acidic/basic sites on the CD surface. These sites provide enhanced chemical reactivity and selective binding capabilities, which are paramount for specific recognition and interaction with target antibiotic molecules, thereby improving sensor selectivity.

5.1.2 Strategic Hybridization with UiO-66 MOF

The second major novelty stems from the intelligent integration of these advanced B,N-codoped CDs with the UiO-66 MOF. This hybridization represents a departure from using standalone sensing materials and offers a powerful synergistic platform:

Overcoming Limitations of Pristine UiO-66: While UiO-66 is renowned for its exceptional stability and high porosity, its intrinsic fluorescence is often weak or non-existent, limiting its direct application as a highly sensitive fluorescence sensor. By encapsulating or integrating highly fluorescent B,N-CDs, the hybrid composite gains a robust and tunable luminescent signaling component, transforming the MOF into an active optical sensing platform.

Mitigating CD Aggregation and Enhancing Stability: Standalone carbon dots can suffer from aggregation in solution, leading to fluorescence quenching and reduced performance. The porous framework of UiO-66 acts as a protective host, physically confining the B,N-CDs within the well-defined pores. This encapsulation prevents aggregation, maintains their dispersed state, and shields them from environmental degradation, thereby preserving and enhancing their fluorescence properties and overall stability in complex matrices.

Enhanced Analyte Pre-concentration: The high surface area and tunable porosity of UiO-66 provide an ideal platform for the pre-concentration of target antibiotic molecules. This MOF-driven enrichment brings the analyte into close proximity with the encapsulated B,N-CDs, significantly increasing the probability of interaction and leading to greatly enhanced sensitivity, particularly for trace-level detection.

5.1.3 Synergistic Sensing Mechanism and Broad Applicability

The combination of B,N-codoped CDs and UiO-66 MOF results in a synergistic sensing mechanism that offers superior performance:

Multi-modal Interactions: The hybrid material leverages a combination of interactions for analyte binding, including hydrogen bonding (between MOF/CD functional groups and antibiotics), electrostatic interactions, π-π stacking (between MOF linkers/CD graphitic domains and aromatic antibiotic structures), and specific interactions with Lewis acidic sites introduced by boron. This multi-modal binding enhances both affinity and selectivity for target antibiotics.

Efficient Fluorescence Modulation: The intimate contact and specific interactions between the pre-concentrated antibiotic and the highly fluorescent B,N-CDs facilitate efficient fluorescence modulation (e.g., through electron transfer or energy transfer mechanisms). This leads to a strong and quantifiable change in the fluorescence signal, enabling ultrasensitive detection.

Robustness in Complex Media: The exceptional chemical and thermal stability of UiO-66, combined with the enhanced photostability of the B,N-CDs, renders the hybrid sensor highly robust. This is crucial for practical applications in real-world complex environmental (e.g., wastewater) and biological (e.g., serum, urine) media, where matrix interferences and harsh conditions can severely impact the performance of less stable sensors.

In conclusion, this study's novelty lies in the rational design and synthesis of a sophisticated hybrid nanomaterial that overcomes the individual limitations of its components. By integrating the unique optical and chemical advantages of B,N-codoped carbon dots with the structural robustness and pre-concentration capabilities of UiO-66 MOF, this research provides a powerful, sensitive, and selective fluorescence sensing platform with significant implications for rapid and accurate antibiotic monitoring in diverse and challenging sample environments.

5.2 Future Directions

Building on the promising results achieved in this study, several avenues can be explored to extend the impact and applicability of the developed B,N-CD@UiO-66 fluorescence sensor:

1. Extension to Other Analytes

Given the versatility of both carbon dots and MOFs, future work could explore the sensor's adaptability for detecting other classes of antibiotics (e.g., tetracyclines, macrolides) or pharmaceutical contaminants in environmental matrices.

2. Surface Functionalization and Post-Synthetic Modifications

Modifying the surface of B,N-CDs with specific ligands or incorporating recognition elements (e.g., aptamers, antibodies) could enhance analyte selectivity and broaden the sensor's utility for biomedical diagnostics.

3. Integration into Portable and On-site Detection Systems

To enable real-time and field-based antibiotic monitoring, integrating the developed sensor into portable or microfluidic devices should be explored. This would enhance the practicality and user-friendliness of the platform in clinical, agricultural, or environmental settings.

4. Scaling-Up and Stability under Harsh Conditions

Efforts toward scaling the synthesis while maintaining reproducibility and performance are necessary for commercial viability. Additionally, evaluating the sensor's performance under extreme conditions (e.g., varying temperatures, high salinity, or acidic pH) would be valuable for broader environmental applications.

5. Toxicity and Biocompatibility Assessment

For future biomedical or food safety applications, a detailed study into the nanocomposite's biocompatibility and toxicity is essential. In vitro or in vivo studies could validate its safety for applications in direct contact with biological systems.

6. Hybrid Sensor Designs

Exploring other MOFs or co-dopant systems (e.g., S,N-CDs, P,N-CDs) could further improve fluorescence output and analyte specificity. Comparative studies could identify the most effective hybrid compositions for diverse sensing needs.

REFERENCES

[1] L. A. Falk, *J Am Med Assoc* 1944, *124*, 1219.

[2] J. B. Haug, *Hospital Antibiotic Use in Norway Epidemiology and Surveillance Methodology*, 2020.

[3] L. O. Omuferen, B. Maseko, J. O. Olowoyo, *Environ Monit Assess* 2022, *194*, 306.

[4] "WHO reports widespread overuse of antibiotics in patients with COVID-19," can be found under https://www.who.int/news/item/26-04-2024-who-reports-widespread-overuse-of-antibiotics-in-patients--hospitalized-with-covid-19, n.d.

[5] "Global, US data show antibiotic use, rise in resistant infections during COVID," can be found under https://www.cidrap.umn.edu/antimicrobial-stewardship/global-us-data-show-high-antibiotic-use-rise-resistant-infections-during, n.d.

[6] S. Rodriguez-Mozaz, S. Chamorro, E. Marti, B. Huerta, M. Gros, A. Sànchez-Melsió, C. M. Borrego, D. Barceló, J. L. Balcázar, *Water Res* 2015, *69*, 234–242.

[7] J. Chen, P. Sun, C.-H. Huang, *Environ Sci Technol* 2016, *50*, 12156–12165.

[8] J. W. Song, J. Bao, Y. Liu, X. Wang, L. Cui, *Chemical Engineering and Processing - Process Intensification* 2024, *198*, 109724.

[9] G. D. Wright, *Curr Opin Microbiol* 2010, *13*, 589–594.

[10] Md. A. Salam, Md. Y. Al-Amin, M. T. Salam, J. S. Pawar, N. Akhter, A. A. Rabaan, M. A. A. Alqumber, *Healthcare* 2023, *11*, 1946.

[11] R. N. Brogden, D. M. Campoli-Richards, *Drugs* 1989, *38*, 524–550.

[12] M. E. Hassouna, *Global Journal of Otolaryngology* 2018, *14*, DOI 10.19080/GJO.2018.14.555886.

[13] M. L. Maheshwari, A. A. Memon, S. Memon, F.-N. Memon, U. U. R. Mughal, A. Dayo, N. Memon, M. A. Ghoto, M. Khan Leghari, *Saudi Pharmaceutical Journal* 2015, *23*, 444–452.

[14] B. Wang, Z. Xu, B. Dong, *J Hazard Mater* 2024, *469*, 133925.

[15] R. Mirzaei, M. Yunesian, S. Nasseri, M. Gholami, E. Jalilzadeh, S. Shoeibi, A. Mesdaghinia, *Science of The Total Environment* 2018, *619–620*, 446–459.

[16] Y. Zeng, F. Chang, Q. Liu, L. Duan, D. Li, H. Zhang, *J Anal Methods Chem* 2022, *2022*, 1–14.

[17] A. N. Koreshkova, V. Gupta, A. Peristyy, C. K. Hasan, P. N. Nesterenko, B. Paull, *J Chromatogr A* 2021, *1640*, 461936.

[18] A. Kumar Mehata, M. N. Lakshmi Suseela, P. Gokul, A. Kumar Malik, M. Kasi Viswanadh, C. Singh, J. Selvin, M. S. Muthu, *Microchemical Journal* 2022, *179*, 107573.

[19] J. Zhang, D. Fu, H. Feng, Y. Li, S. Zhang, C. Peng, Y. Wang, H. Sun, L. Wang, *TrAC Trends in Analytical Chemistry* 2024, *170*, 117472.

[20] D. Krakkó, V. Licul-Kucera, G. Záray, V. G. Mihucz, *Microchemical Journal* 2019, *148*, 108–119.

[21] A. M. García-Campaña, L. Gámiz-Gracia, F. J. Lara, M. del Olmo Iruela, C. Cruces-Blanco, *Anal Bioanal Chem* 2009, *395*, 967–986.

[22] K. A. S. Fernando, S. Sahu, Y. Liu, W. K. Lewis, E. A. Guliants, A. Jafariyan, P. Wang, C. E. Bunker, Y.-P. Sun, *ACS Appl Mater Interfaces* 2015, *7*, 8363–8376.

[23] B. Garg, T. Bisht, *Molecules* 2016, *21*, 1653.

[24] J. Dong, X. Han, Y. Liu, H. Li, Y. Cui, *Angewandte Chemie International Edition* 2020, *59*, 13722–13733.

[25] X. Zhu, J. Zhang, J. Liu, Y. Zhang, *Advanced Science* 2019, *6*, DOI 10.1002/advs.201901358.

[26] V. V Butova, M. A. Soldatov, A. A. Guda, K. A. Lomachenko, C. Lamberti, *Russian Chemical Reviews* 2016, *85*, 280–307.

[27] X. Zhang, Z. Chen, X. Liu, S. L. Hanna, X. Wang, R. Taheri-Ledari, A. Maleki, P. Li, O. K. Farha, *Chem Soc Rev* 2020, *49*, 7406–7427.

[28] O. M. Yaghi, H. Li, *J Am Chem Soc* 1995, *117*, 10401–10402.

[29] O. M. Yaghi, G. Li, H. Li, *Nature* 1995, *378*, 703–706.

[30] P. Z. Moghadam, A. Li, X.-W. Liu, R. Bueno-Perez, S.-D. Wang, S. B. Wiggin, P. A. Wood, D. Fairen-Jimenez, *Chem Sci* 2020, *11*, 8373–8387.

[31] E. Sharmin, F. Zafar, in *Metal-Organic Frameworks*, InTech, 2016.

[32] L. Zhu, D. Zhang, M. Xue, H. Li, S. Qiu, *CrystEngComm* 2013, *15*, 9356.

[33] J. L. C. Rowsell, O. M. Yaghi, *Microporous and Mesoporous* 2004, *73*, 3–14.

[34] H. Deng, S. Grunder, K. E. Cordova, C. Valente, H. Furukawa, M. Hmadeh, F. Gándara, A. C. Whalley, Z. Liu, S. Asahina, H. Kazumori, M. O'Keeffe, O. Terasaki, J. F. Stoddart, O. M. Yaghi, *Science (1979)* 2012, *336*, 1018–1023.

[35] H. Furukawa, K. E. Cordova, M. O'Keeffe, O. M. Yaghi, *Science (1979)* 2013, *341*, DOI 10.1126/science.1230444.

[36] H. Furukawa, Y. B. Go, N. Ko, Y. K. Park, F. J. Uribe-Romo, J. Kim, M. O'Keeffe, O. M. Yaghi, *Inorg Chem* 2011, *50*, 9147–9152.

[37] A. Rapeyko, J. C. Díaz Infante, F. X. Llabrés i Xamena, *Mol Syst Des Eng* 2023, *8*, 775–785.

[38] K. K. Tanabe, S. M. Cohen, *Chem. Soc. Rev.* 2011, *40*, 498–519.

[39] T. Saeed, A. Naeem, I. Ud Din, M. A. Alotaibi, A. I. Alharthi, I. Wali Khan, N. Huma Khan, T. Malik, *Microchemical Journal* 2020, *159*, 105579.

[40] M. Taddei, P. V. Dau, S. M. Cohen, M. Ranocchiari, J. A. van Bokhoven, F. Costantino, S. Sabatini, R. Vivani, *Dalton Transactions* 2015, *44*, 14019–14026.

[41] C. Chen, D. Chen, S. Xie, H. Quan, X. Luo, L. Guo, *ACS Appl Mater Interfaces* 2017, *9*, 41043–41054.

[42] T. Wang, Y. Xia, X. Wan, Y. Zhang, N. Chen, Y. Jin, G. Li, *Microchemical Journal* 2024, *201*, 110673.

[43] Y.-H. Li, C.-C. Wang, X.-H. Yi, H.-Y. Chu, *Environmental Functional Materials* 2023, *2*, 93–132.

[44] J. H. Cavka, S. Jakobsen, U. Olsbye, N. Guillou, C. Lamberti, S. Bordiga, K. P. Lillerud, *J Am Chem Soc* 2008, *130*, 13850–13851.

[45] R. M. Rego, M. D. Kurkuri, M. Kigga, *Chemosphere* 2022, *302*, 134845.

[46] J.-M. Yang, X.-W. Hu, Y.-X. Liu, W. Zhang, *Microporous and Mesoporous Materials* 2019, *274*, 149–154.

[47] Z. Wang, B. Yao, Y. Xiao, X. Tian, Y. Wang, *Chemosensors* 2023, *11*, 405.

[48] L. Zou, Z. Gu, M. Sun, *Toxicol Environ Chem* 2015, *97*, 477–490.

[49] A. Panja, P. Patra, *4open* 2023, *6*, 1.

[50] F. P. García de Arquer, D. V. Talapin, V. I. Klimov, Y. Arakawa, M. Bayer, E. H. Sargent, *Science (1979)* 2021, *373*, DOI 10.1126/science.aaz8541.

[51] D. Ozyurt, M. Al Kobaisi, R. K. Hocking, B. Fox, *Carbon Trends* 2023, *12*, 100276.

[52] P. Hawrylak, in *Optical Properties of Semiconductor Nanostructures*, Springer Netherlands, Dordrecht, 2000, pp. 319–336.

[53] A. D. Yoffe, *Adv Phys* 2001, *50*, 1–208.

[54] S. M. Reimann, M. Manninen, *Rev Mod Phys* 2002, *74*, 1283–1342.

[55] K. Sanderson, *Nature* 2009, *459*, 760–761.

[56] Y. He, H. Lu, L. Sai, Y. Su, M. Hu, C. Fan, W. Huang, L. Wang, *Advanced Materials* 2008, *20*, 3416–3421.

[57] V. G. Reshma, P. V. Mohanan, *J Lumin* 2019, *205*, 287–298.

[58] A. Kaur, K. Pandey, R. Kaur, N. Vashishat, M. Kaur, *Chemosensors* 2022, *10*, 367.

[59] C. Deng, T. Fu, Q. Huang, Z. Fu, Y. Lu, *J Lumin* 2024, *267*, 120395.

[60] S. B. Rizvi, S. Ghaderi, M. Keshtgar, A. M. Seifalian, *Nano Rev* 2010, *1*, 5161.

[61] Q. Ma, X. Su, *Analyst* 2011, *136*, 4883.

[62] Z. Ramezani, F. K. Ghalehsardi, S. Noorizadeh, in *Quantum Dots in Bioanalytical Chemistry and Medicine*, Royal Society Of Chemistry, 2023, pp. 1–36.

[63] M. M. Sabzehmeidani, M. Kazemzad, *Science of The Total Environment* 2022, *810*, 151997.

[64] V. D. Dang, A. B. Ganganboina, R.-A. Doong, *ACS Appl Mater Interfaces* 2020, *12*, 32247–32258.

[65] K. Ren, S.-H. Wu, X.-F. Guo, H. Wang, *Inorg Chem* 2019, *58*, 4223–4229.

[66] C. Guo, A. C. Sedgwick, T. Hirao, J. L. Sessler, *Coord Chem Rev* 2021, *427*, 213560.

[67] D. Wu, A. C. Sedgwick, T. Gunnlaugsson, E. U. Akkaya, J. Yoon, T. D. James, *Chem Soc Rev* 2017, *46*, 7105–7123.

[68] S.-H. Park, N. Kwon, J.-H. Lee, J. Yoon, *Chem Soc Rev* 2020, *49*, 143–179.

[69] Z. Zhang, H. Zhang, D. Tian, A. Phan, M. Seididamyeh, M. Alanazi, Z. Ping Xu, Y. Sultanbawa, R. Zhang, *Coord Chem Rev* 2024, *498*, 215455.

[70] K. Agarwal, H. Rai, S. Mondal, *Mater Res Express* 2023, *10*, 062001.

[71] Y. Yulong, P. Xinsheng, *Analyst* 2016, *141*, 2619–2628.

[72] A. Das, P. T. Snee, *ChemPhysChem* 2016, *17*, 598–617.

[73] Y. Wang, H. Wang, J. Guo, J. Wu, L. J. Gao, Y. H. Sun, J. Zhao, G. F. Zou, *Nanoscale Res Lett* 2015, *10*, 300.

[74] Y. Zhang, Y. Shen, X. Wang, L. Zhu, B. Han, L. Ge, Y. Tao, A. Xie, *Mater Lett* 2012, *78*, 35–38.

[75] H. Qi, M. Teng, M. Liu, S. Liu, J. Li, H. Yu, C. Teng, Z. Huang, H. Liu, Q. Shao, A. Umar, T. Ding, Q. Gao, Z. Guo, *J Colloid Interface Sci* 2019, *539*, 332–341.

[76] K. Yong, W. Law, I. Roy, Z. Jing, H. Huang, M. T. Swihart, P. N. Prasad, *J Biophotonics* 2011, *4*, 9–20.

[77] X. Xu, Y. Yang, H. Jin, B. Pang, R. Yang, L. Yan, C. Jiang, D. Shao, J. Shi, *ACS Sustain Chem Eng* 2020, *8*, 6806–6814.

[78] H. Lu, H. Zhang, Y. Li, F. Gan, *RSC Adv* 2021, *11*, 22960–22968.

[79] M. Hou, X. Yan, L. Xiong, *J Lumin* 2015, *157*, 58–62.

[80] X.-D. Zhu, K. Zhang, Y. Wang, W.-W. Long, R.-J. Sa, T.-F. Liu, J. Lü, *Inorg Chem* 2018, *57*, 1060–1065.

[81] J.-H. Qin, Y.-D. Huang, M.-Y. Shi, H.-R. Wang, M.-L. Han, X.-G. Yang, F.-F. Li, L.-F. Ma, *RSC Adv* 2020, *10*, 1439–1446.

[82] Y. Zhou, Q. Yang, D. Zhang, N. Gan, Q. Li, J. Cuan, *Sens Actuators B Chem* 2018, *262*, 137–143.

[83] C. Li, L. Zhu, W. Yang, X. He, S. Zhao, X. Zhang, W. Tang, J. Wang, T. Yue, Z. Li, *J Agric Food Chem* 2019, *67*, 1277–1283.

[84] M. Lei, F. Ge, S. Ren, X. Gao, H. Zheng, *Sep Purif Technol* 2022, *286*, 120433.

[85] S. Zhou, L. Lu, D. Liu, J. Wang, H. Sakiyama, Mohd. Muddassir, A. Nezamzadeh-Ejhieh, J. Liu, *CrystEngComm* 2021, *23*, 8043–8052.

[86] X. Dou, K. Sun, H. Chen, Y. Jiang, L. Wu, J. Mei, Z. Ding, J. Xie, *Antibiotics* 2021, *10*, 358.

[87] A. Lan, K. Li, H. Wu, D. H. Olson, T. J. Emge, W. Ki, M. Hong, J. Li, *Angewandte Chemie International Edition* 2009, *48*, 2334–2338.

[88] K. Binnemans, *Chem Rev* 2009, *109*, 4283–4374.

[89] M. D. Allendorf, C. A. Bauer, R. K. Bhakta, R. J. T. Houk, *Chem Soc Rev* 2009, *38*, 1330.

[90] X.-Q. Zhao, B. Zhao, W. Shi, P. Cheng, *CrystEngComm* 2009, *11*, 1261.

[91] B. Zhao, X.-Q. Zhao, Z. Chen, W. Shi, P. Cheng, S.-P. Yan, D.-Z. Liao, *CrystEngComm* 2008, *10*, 1144.

[92] A. C. Wibowo, S. A. Vaughn, M. D. Smith, H.-C. zur Loye, *Inorg Chem* 2010, *49*, 11001–11008.

[93] K. C. Stylianou, R. Heck, S. Y. Chong, J. Bacsa, J. T. A. Jones, Y. Z. Khimyak, D. Bradshaw, M. J. Rosseinsky, *J Am Chem Soc* 2010, *132*, 4119–4130.

[94] Q. Yu, Z. Li, Q. Cao, S. Qu, Q. Jia, *TrAC Trends in Analytical Chemistry* 2020, *129*, 115939.

[95] H. He, Y. Cui, B. Li, B. Wang, C. Jin, J. Yu, L. Yao, Y. Yang, B. Chen, G. Qian, *Advanced Materials* 2019, *31*, DOI 10.1002/adma.201806897.

[96] R. Kaur, A. Rana, R. K. Singh, V. A. Chhabra, K.-H. Kim, A. Deep, *RSC Adv* 2017, *7*, 29015–29024.

[97] B.-H. Wang, B. Yan, *CrystEngComm* 2019, *21*, 4637–4643.

[98] Q. Fang, G. Zhu, Z. Jin, Y. Ji, J. Ye, M. Xue, H. Yang, Y. Wang, S. Qiu, *Angewandte Chemie International Edition* 2007, *46*, 6638–6642.

[99] Y. Cui, R. Song, J. Yu, M. Liu, Z. Wang, C. Wu, Y. Yang, Z. Wang, B. Chen, G. Qian, *Advanced Materials* 2015, *27*, 1420–1425.

[100] A. Bigdeli, F. Ghasemi, H. Golmohammadi, S. Abbasi-Moayed, M. A. F. Nejad, N. Fahimi-Kashani, S. Jafarinejad, M. Shahrajabian, M. R. Hormozi-Nezhad, *Nanoscale* 2017, *9*, 16546–16563.

[101] J. Zhang, Y. Huang, D. Yue, Y. Cui, Y. Yang, G. Qian, *J Mater Chem B* 2018, *6*, 5174–5180.

[102] A. H. Malik, P. K. Iyer, *ACS Appl Mater Interfaces* 2017, *9*, 4433–4439.

[103] C. Du, Z. Zhang, G. Yu, H. Wu, H. Chen, L. Zhou, Y. Zhang, Y. Su, S. Tan, L. Yang, J. Song, S. Wang, *Chemosphere* 2021, *272*, 129501.

[104] X. Zhao, M. Zheng, X. Gao, J. Zhang, E. Wang, Z. Gao, *Coord Chem Rev* 2021, *440*, 213970.

[105] J. Liu, Q. Li, F. Mao, K. Wang, H. Wu, *Chem Asian J* 2021, *16*, 3585–3598.

[106] Z. Hasan, S. H. Jhung, *J Hazard Mater* 2015, *283*, 329–339.

[107] A. Khezerlou, M. Tavassoli, B. Khalilzadeh, A. Ehsani, H. Kazemian, *Food Control* 2023, *153*, 109965.

[108] T. Gan, X. Zhang, G. Qin, Y. Ni, *J Mater Chem C Mater* 2022, *10*, 1517–1525.

[109] W. Cao, Y. Zhang, Z. Shi, T. Liu, X. Song, L. Zhang, P. Keung Wong, Z. Chen, *Chemical Engineering Journal* 2021, *417*, 128112.

[110] C. Wang, C. Xiong, X. Zhang, Y. He, J. Xu, Y. Zhao, S. Wang, J. Zheng, *Sep Purif Technol* 2022, *296*, 121329.

[111] M. S. Embaby, S. D. Elwany, W. Setyaningsih, M. R. Saber, *Chin J Chem Eng* 2018, *26*, 731–739.

[112] S. Ali, Z. Zuhra, Y. Abbas, Y. Shu, M. Ahmad, Z. Wang, *Langmuir* 2021, *37*, 13602–13609.

[113] T. Guan, X. Li, W. Fang, D. Wu, *Appl Surf Sci* 2020, *501*, 144074.

[114] Y. Zhao, D. Wang, W. Wei, L. Cui, C.-W. Cho, G. Wu, *Environmental Science and Pollution Research* 2021, *28*, 7068–7075.

[115] Alamgir, K. Talha, B. Wang, J.-H. Liu, R. Ullah, F. Feng, J. Yu, S. Chen, J.-R. Li, *J Environ Chem Eng* 2020, *8*, 103642.

[116] J. Cao, Z. Yang, W. Xiong, Y. Zhou, Y. Peng, X. Li, C. Zhou, R. Xu, Y. Zhang, *Chemical Engineering Journal* 2018, *353*, 126–137.

[117] F. Nouar, M. I. Breeze, B. C. Campo, A. Vimont, G. Clet, M. Daturi, T. Devic, R. I. Walton, C. Serre, *Chemical Communications* 2015, *51*, 14458–14461.

[118] X. Min, X. Wu, P. Shao, Z. Ren, L. Ding, X. Luo, *Chemical Engineering Journal* 2019, *358*, 321–330.

[119] M. Qin, Y. Shi, D. Lu, J. Deng, G. Shi, T. Zhou, *Appl Surf Sci* 2022, *595*, 153494.

[120] J. Low, J. Yu, M. Jaroniec, S. Wageh, A. A. Al-Ghamdi, *Advanced Materials* 2017, *29*, DOI 10.1002/adma.201601694.

[121] Z. Wang, Z. Lin, S. Shen, W. Zhong, S. Cao, *Chinese Journal of Catalysis* 2021, *42*, 710–730.

[122] K. Wang, J. Wu, M. Zhu, Y.-Z. Zheng, X. Tao, *J Solid State Chem* 2020, *284*, 121200.

[123] X. Wang, X. Wang, *RSC Adv* 2022, *12*, 23427–23436.

[124] M. L. Liu, B. Bin Chen, C. M. Li, C. Z. Huang, *Green Chemistry* 2019, *21*, 449–471.

[125] L. Li, T. Dong, *J Mater Chem C Mater* 2018, *6*, 7944–7970.

[126] S. Zhu, Y. Song, X. Zhao, J. Zhang, B. Yang, *Nano Res* 2015, *8*, 355–381.

[127] C. Xia, S. Zhu, T. Feng, M. Yang, B. Yang, *Advanced Science* 2019, *6*, DOI 10.1002/advs.201901316.

[128] M. G. Giordano, G. Seganti, M. Bartoli, *Molecules* 2023, *28*, 2772.

[129] M. Shamsipur, A. Barati, A. A. Taherpour, M. Jamshidi, *J Phys Chem Lett* 2018, *9*, 4189–4198.

[130] H.-W. Chu, B. Unnikrishnan, A. Anand, Y.-W. Lin, C.-C. Huang, *J Food Drug Anal* 2020, *28*, 540–558.

[131] S. Setianto, L. K. Men, A. Bahtiar, C. Panatarani, *Sci Rep* 2024, *14*, 1996.

[132] L. Feng, X.-Y. Tang, Y.-X. Zhong, Y.-W. Liu, X.-H. Song, S.-L. Deng, S.-Y. Xie, J.-W. Yan, L.-S. Zheng, *Nanoscale* 2014, *6*, 12635–12643.

[133] P. Zhao, L. Zhu, *Chemical Communications* 2018, *54*, 5401–5406.

[134] M. A. Mousa, H. H. Abdelrahman, M. A. Fahmy, D. G. Ebrahim, A. H. E. Moustafa, *Sci Rep* 2023, *13*, 12863.

[135] Y. Park, J. Yoo, B. Lim, W. Kwon, S.-W. Rhee, *J Mater Chem A Mater* 2016, *4*, 11582–11603.

[136] P. Kumar, S. Dua, R. Kaur, M. Kumar, *RSC Adv* 2022, *12*, 4714–4759.

[137] I. SINGH, R. ARORA, H. DHIMAN, R. PAHWA, *The Turkish Journal of Pharmaceutical Sciences* 2018, *15*, 219–230.

[138] K. Chang, Q. Zhu, L. Qi, M. Guo, W. Gao, Q. Gao, *Materials* 2022, *15*, 466.

[139] N. Nammahachak, K. K. Aup-Ngoen, P. Asanithi, M. Horpratum, S. Chuangchote, S. Ratanaphan, W. Surareungchai, *RSC Adv* 2022, *12*, 31729–31733.

[140] G. S. Jamila, S. Sajjad, S. A. K. Leghari, T. Kallio, C. Flox, *J Nanostructure Chem* 2022, *12*, 611–623.

[141] G. Henriquez, J. Ahlawat, R. Fairman, M. Narayan, *ACS Chem Neurosci* 2022, *13*, 2399–2409.

[142] Y. Qu, X. Li, H. Zhang, R. Huang, W. Qi, R. Su, Z. He, *J Hazard Mater* 2022, *429*, 128310.

[143] Y. Qiu, D. Li, Y. Li, X. Ma, J. Li, *Cellulose* 2022, *29*, 367–378.

[144] A. Kundu, B. Maity, S. Basu, *ACS Biomater Sci Eng* 2022, *8*, 4764–4776.

[145] H. M. E. M. El-brolsy, N. A. N. Hanafy, M. A. El-Kemary, *Int J Mol Sci* 2022, *23*, 13283.

[146] L. Yao, M.-M. Zhao, Q.-W. Luo, Y.-C. Zhang, T.-T. Liu, Z. Yang, M. Liao, P. Tu, K.-W. Zeng, *ACS Nano* 2022, *16*, 9228–9239.

[147] M. Kumari, G. R. Chaudhary, S. Chaudhary, A. Umar, S. Akbar, S. Baskoutas, *Molecules* 2022, *27*, 5329.

[148] P. K. Yadav, S. Chandra, V. Kumar, D. Kumar, S. H. Hasan, *Catalysts* 2023, *13*, 422.

[149] Z. Sun, Y. Zhou, W. Zhou, J. Luo, R. Liu, X. Zhang, L. Zhou, Q. Pang, *Nanoscale* 2021, *13*, 2472–2480.

[150] F. Wang, Y. Zhang, H. Li, W. Gong, J. Han, S. Jiang, D. Li, Z. Yao, *Food Chem* 2025, *463*, 141122.

[151] Z. Zhang, Y. Pan, Y. Fang, L. Zhang, J. Chen, *Nanoscale* 2016, *8*, 500–507.

[152] F. Yan, Y. Jiang, X. Sun, Z. Bai, Y. Zhang, X. Zhou, *Microchimica Acta* 2018, *185*, 424.

[153] F. Zu, F. Yan, Z. Bai, J. Xu, Y. Wang, Y. Huang, X. Zhou, *Microchimica Acta* 2017, *184*, 1899–1914.

[154] M. E. El Sharkasy, M. M. Tolba, F. Belal, M. I. Walash, R. Aboshabana, *Spectrochim Acta A Mol Biomol Spectrosc* 2023, *289*, 122246.

[155] J. Huang, C. Long, L. Zhang, T. Qing, P. Zhang, Z. Qing, B. Feng, *J Environ Chem Eng* 2022, *10*, 108951.

[156] D. Bradshaw, A. Garai, J. Huo, *Chem. Soc. Rev.* 2012, *41*, 2344–2381.

[157] C. Petit, B. Mendoza, T. J. Bandosz, *Langmuir* 2010, *26*, 15302–15309.

[158] Y. Zhang, M. Sun, M. Peng, E. Du, X. Xu, C.-C. Wang, *Chinese Chemical Letters* 2023, *34*, 107478.

[159] R. Jalili, M. H. Irani-nezhad, A. Khataee, S. W. Joo, *Spectrochim Acta A Mol Biomol Spectrosc* 2021, *262*, 120089.

[160] Y. Tao, Y. Jiang, Y. Huang, J. Liu, P. Zhang, X. Chen, Y. Fan, L. Wang, J. Xu, *CrystEngComm* 2021, *23*, 4038–4049.

[161] N. Khansili, *Environmental Advances* 2024, *16*, 100542.

[162] L. Cui, X. Ren, M. Sun, H. Liu, L. Xia, *Nanomaterials* 2021, *11*, 3419.

[163] Q.-L. Zhu, Q. Xu, *Chem. Soc. Rev.* 2014, *43*, 5468–5512.

[164] N. Stock, S. Biswas, *Chem Rev* 2012, *112*, 933–969.

[165] B. Li, T. Suo, S. Xie, A. Xia, Y. Ma, H. Huang, X. Zhang, Q. Hu, *TrAC Trends in Analytical Chemistry* 2021, *135*, 116163.

[166] Z. Wang, X. Jin, L. Yan, Y. Yang, X. Liu, *Microchimica Acta* 2023, *190*, 28.

[167] X. Fu, R. Lv, J. Su, H. Li, B. Yang, X. Liu, *RSC Adv* 2018, *8*, 4766–4772.

[168] N. Wang, M. Xie, M. Wang, Z. Li, X. Su, *Talanta* 2020, *220*, 121352.

[169] Z. Lin, Q. Zeng, Q. Deng, W. Yao, H. Deng, X. Lin, W. Chen, *Sens Actuators B Chem* 2022, *359*, 131563.

[170] S. Wu, W. Li, M. Zheng, Y. Zheng, Q. Li, J. Liang, J. Chen, X. Huang, Y. Liu, X. Zhang, B. Lei, *Microporous and Mesoporous Materials* 2022, *345*, 112254.

[171] D. Wu, Y. Liu, Y. Wu, B. Tan, *Dalton Transactions* 2018, *47*, 5961–5967.

[172] M. Nasrabadi, M. A. Ghasemzadeh, M. R. Zand Monfared, *New Journal of Chemistry* 2019, *43*, 16033–16040.

[173] C. Gu, Q. Wang, L. Zhang, P. Yang, *Sens Actuators B Chem* 2020, *305*, 127478.

[174] P. G. González, Y. B. Pliego-Cuervo, *Chemical Engineering Research and Design* 2014, *92*, 2715–2724.

[175] K. J. Mintz, M. Bartoli, M. Rovere, Y. Zhou, S. D. Hettiarachchi, S. Paudyal, J. Chen, J. B. Domena, P. Y. Liyanage, *Carbon N Y* 2021, *173*, 433–447.

[176] Z. Yang, M. Xu, Y. Liu, F. He, F. Gao, Y. Su, H. Wei, Y. Zhang, *Nanoscale* 2014, *6*, 1890–1895.

[177] P. C. Lemaire, D. T. Lee, J. Zhao, G. N. Parsons, *ACS Appl Mater Interfaces* 2017, *9*, 22042–22054.

[178] Y. Luan, Y. Qi, H. Gao, R. S. Andriamitantsoa, N. Zheng, G. Wang, *J Mater Chem A Mater* 2015, *3*, 17320–17331.

[179] S. Feng, Z. Ni, S. Feng, Z. Zhang, S. Liu, R. Wang, J. Hu, *J Radioanal Nucl Chem* 2019, *319*, 737–748.

[180] F. Yang, S. Xie, G. Wang, C. W. Yu, H. Liu, Y. Liu, *Environmental Science and Pollution Research* 2020, *27*, 20246–20258.

[181] Y. Wang, N. Zhang, D. Chen, D. Ma, G. Liu, X. Zou, Y. Chen, R. Shu, Q. Song, W. Lv, *Science of The Total Environment* 2019, *682*, 118–127.

[182] S. Wu, C. Chen, J. Chen, W. Li, J. Zhuang, J. Lin, Y. Liu, H. Xu, M. Zheng, X. Zhang, B. Lei, H. Zhang, *J Mater Chem C Mater* 2022, *10*, 15508–15515.

[183] Z. Ren, W. Guo, S. Sun, X. Liu, Z. Fan, F. Wang, A. A. Ibrahim, A. Umar, A. A. M. Alkhanjaf, S. Baskoutas, *Microchimica Acta* 2023, *190*, 438.

[184] Y. Li, Y. Shen, Y. Zhang, T. Zeng, Q. Wan, G. Lai, N. Yang, *Anal Chim Acta* 2021, *1158*, 338419.

[185] Z. Peng, Y. Zhou, C. Ji, J. Pardo, K. J. Mintz, R. R. Pandey, C. C. Chusuei, R. M. Graham, G. Yan, R. M. Leblanc, *Nanomaterials* 2020, *10*, 1560.

[186] L. Cao, M. Zan, F. Chen, X. Kou, Y. Liu, P. Wang, Q. Mei, Z. Hou, W.-F. Dong, L. Li, *Carbon N Y* 2022, *194*, 42–51.

[187] M. Peñas-Garzón, M. J. Sampaio, Y. L. Wang, J. Bedia, J. J. Rodriguez, C. Belver, C. G. Silva, J. L. Faria, *Sep Purif Technol* 2022, *286*, 120467.

[188] J. Xu, Z. Zhao, Y. Cao, H. Huang, R. Shen, C. Zeng, J. Lv, C. Qi, Z. Lei, H. Feng, H. Ma, *Chem Asian J* 2025, *20*, DOI 10.1002/asia.202401138.

[189] S. Xing, K. Zheng, L. Shi, K. Kang, Z. Peng, X. Zhang, B. Liu, H. Yang, G. Yue, *Molecules* 2024, *29*, 1662.

[190] T. K. Vo, V. N. Le, V. C. Nguyen, M. Song, D. Kim, K. S. Yoo, B. J. Park, J. Kim, *Journal of Industrial and Engineering Chemistry* 2020, *86*, 178–185.

[191] L. Ai, Y. Yang, B. Wang, J. Chang, Z. Tang, B. Yang, S. Lu, *Sci Bull (Beijing)* 2021, *66*, 839–856.

[192] S. Sun, M. Liu, X.-T. Jin, J. Zhao, Y.-H. Luo, *Spectrochim Acta A Mol Biomol Spectrosc* 2025, *326*, 125187.

[193] M. Yu, Y. Xie, X. Wang, Y. Li, G. Li, *ACS Appl Mater Interfaces* 2019, *11*, 21201–21210.

[194] G. E. LeCroy, F. Messina, A. Sciortino, P. Wang, K. A. S. Fernando, Y.-P. Sun, *The Journal of Physical Chemistry C* 2017, *121*, 28180–28186.

[195] X. Li, J. Wu, *Spectrochim Acta A Mol Biomol Spectrosc* 2024, *307*, 123662.

[196] G. Qin, J. Wang, L. Li, F. Yuan, W. Bai, Y. Ni, *Talanta* 2021, *221*, 121421.

[197] X. Wang, C. Liu, Y. Cao, L. Cai, H. Wang, G. Fang, *Foods* 2023, *12*, 2255.

[198] Y. Zhang, Y. Lu, M. Sun, D. Zeng, *Water (Basel)* 2023, *16*, 145.

[199] M. Haddad Irani-nezhad, R. Jalili, E. Kohan, A. Khataee, Y. Yoon, *Environ Res* 2022, *205*, 112512.

[200] Y. Zheng, H. Yang, Q. Yang, Y. Li, P. G. Karmaker, X. Yang, *Dyes and Pigments* 2024, *230*, 112340.

[201] F. Akhgari, N. Samadi, K. Farhadi, *J Fluoresc* 2017, *27*, 921–927.

[202] H. Pan, S. Wang, X. Dao, Y. Ni, *Inorg Chem* 2018, *57*, 1417–1425.

[203] M. Haddad Irani-nezhad, R. Jalili, E. Kohan, A. Khataee, Y. Yoon, *Environ Res* 2022, *205*, 112512.

[204] Y. Zheng, H. Yang, Q. Yang, Y. Li, P. G. Karmaker, X. Yang, *Dyes and Pigments* 2024, *230*, 112340.

[205] H. Pan, S. Wang, X. Dao, Y. Ni, *Inorg Chem* 2018, *57*, 1417–1425.

[206] G. Qin, J. Wang, L. Li, F. Yuan, Q. Zha, W. Bai, Y. Ni, *Talanta* 2021, *221*, DOI 10.1016/j.talanta.2020.121421.

[207] F. Akhgari, N. Samadi, *J Fluoresc* 2017, *27*, DOI 10.1007/s10895-017-2027-0.

[208] Z.-W. Zhai, S.-H. Yang, M. Cao, L.-K. Li, C.-X. Du, S.-Q. Zang, *Cryst Growth Des* 2018, *18*, 7173–7182.